High A-scan rate optical coherence tomography angiography for blood flow speed quantification in the retina

By

Yunchan Hwang

B.S. in Electrical and Computer Engineering, Seoul National University (2020)

Submitted to the Department of Electrical Engineering and Computer Science in Partial Fulfillment of the Requirements for the Degree of

Master of Science

at the

MASSACHUSETTS INSTITUTE OF TECHNOLOGY

February 2024

Authored by:	Yunchan Hwang Department of Electrical Engineering and Computer Science December 29, 2023
Certified by:	James G. Fujimoto Elihu Thomson Professor of Electrical Engineering and Computer Science Thesis Supervisor
Accepted by:	Leslie A. Kolodziejski Professor of Electrical Engineering and Computer Science Chair, Department Committee on Graduate Students

High A-scan rate optical coherence tomography angiography for blood flow speed quantification in the retina

by

Yunchan Hwang

Submitted to the Department of Electrical Engineering
and Computer Science on December 29, 2023 in
Partial Fulfillment of the Requirements for the Degree
of Master of Science in Electrical Engineering and
Computer Science

Abstract

Optical coherence tomography angiography (OCTA) offers non-invasive and depth-resolved imaging of the retinal vasculature. While OCTA is widely used to study retinal disease, it traditionally provides limited information about blood flow speed. This thesis introduces a second-generation variable interscan time analysis (VISTA) OCTA, designed to evaluate a quantitative surrogate marker for blood flow speed in the vasculature. At the capillary level, spatially compiled OCTA and a simple temporal autocorrelation model, $\rho(\tau) = \exp(-\alpha\tau)$, are used to evaluate a temporal autocorrelation decay constant, α, as a marker for blood flow speed. A 600 kHz A-scan rate swept-source OCT prototype instrument provides short interscan time OCTA and fine A-scan spacing acquisition, while maintaining multi mm^2 field-of-views for human retinal imaging. The cardiac pulsatility in α is demonstrated and its synchronization across retinal capillaries is quantified. The repeatability of α measurements is evaluated at multiple spatial levels. This new approach reveals varying α values across different retinal capillary plexuses in healthy eyes, and demonstrates spatial correspondence between high blood flow speeds and the centers of choriocapillaris lobules. VISTA OCTA images of eyes with diabetic retinopathy and age-related macular degeneration are also presented. By providing blood flow speed information, the second-generation VISTA aims to enhance and complement traditional structural vasculature imaging offered by OCTA. These advancements promise to enable clinical studies of blood flow speed alterations in retinal diseases, offering earlier markers for disease detection, progression, and response to treatment.

Thesis Supervisor: James G. Fujimoto

Title: Elihu Thomson Professor of Electrical Engineering

Table of Contents

Chapter 1

Introduction

1.1 Normal retinal vasculature

The retina is a light-sensitive layer that is responsible for visual perception. It is the innermost tissue of the eye composed of multiple layers, each containing different types of neurons. External light is focused onto the retina by the cornea and the lens, and the light is detected by photoreceptors. The signals from the photoreceptors are propagated and processed through different neuronal cells and finally transmitted to the brain. These various neurons are responsible for the stratified layer structure of the retina. Figure 1.1 illustrates the retina's layered structure, with annotations for each layer, and the fovea, a small depression in the retina where the high acuity vision is achieved.

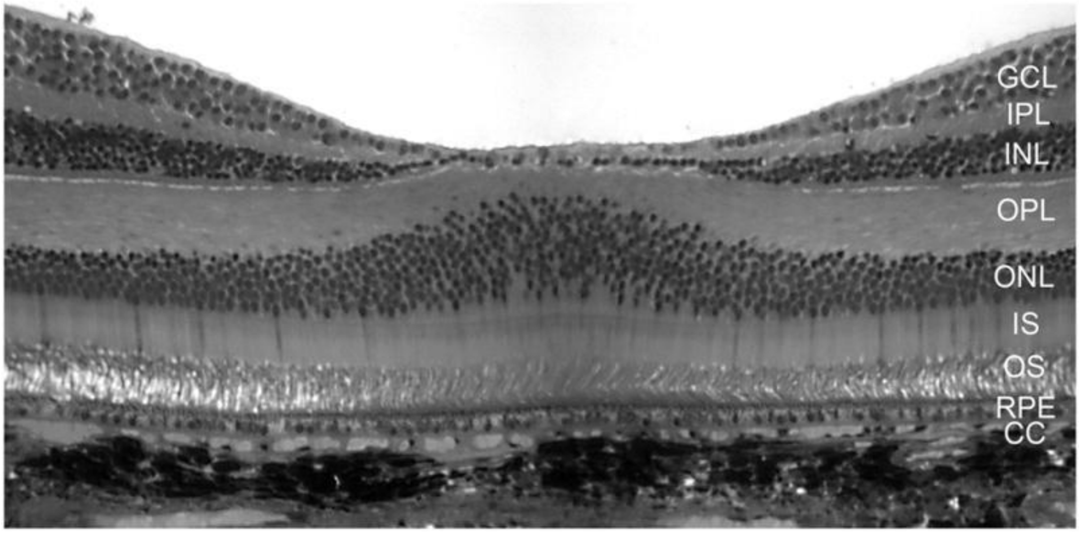

Figure 1.1. A layered structure of the retina. The image is a histology of a fovea from a Macaque monkey. Different retinal layers are annotated on the right. GCL: ganglion cell layer. IPL: inner plexiform layer. INL: inner nuclear layer. OPL: outer plexiform layer. ONL: outer nuclear layer. IS: inner segment of photoreceptors. OS: outer segment of photoreceptors. RPE: retinal pigment epithelium. CC: choriocapillaris. From reference [1].

As a part of the central nervous system, the retina has high and dynamic metabolic demands, and different retinal layers are thought to have different metabolisms. The retina is supplied by two different vasculatures: retinal vasculature and choroidal vasculature. The retinal vasculature is supplied by the central retinal artery and features multiple capillary plexuses embedded in the inner retina, which is between the inner limiting membrane and the external limiting membrane. The choroidal vasculature, supplied by the posterior ciliary arteries, is situated posterior to the Bruch’s membrane.

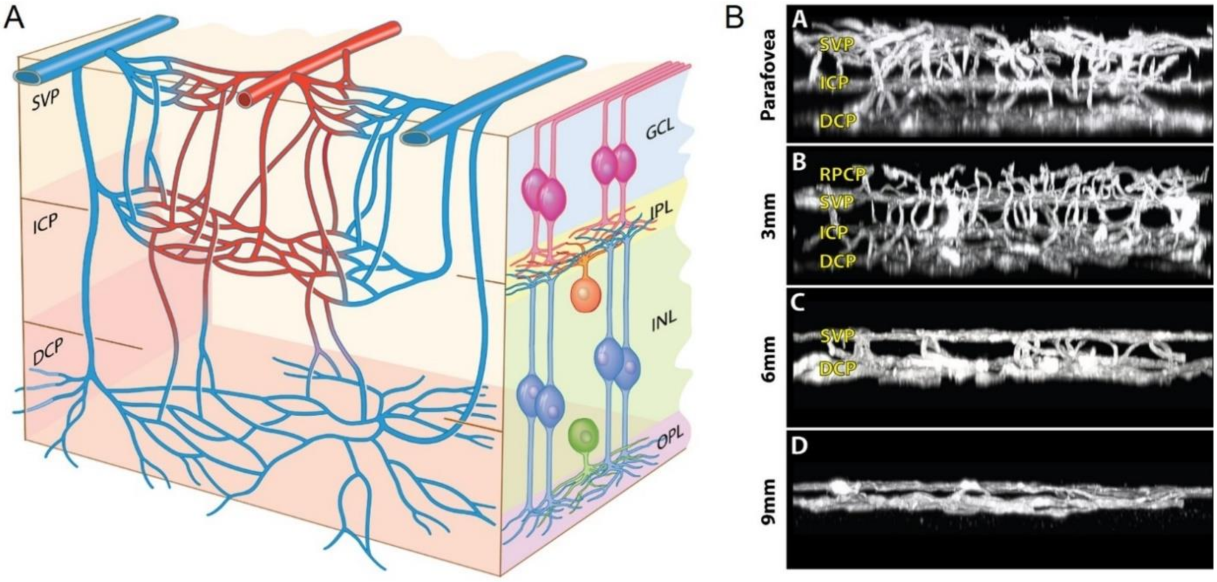

Figure 1.2. Retinal vasculature. (A) Schematic of multiple plexuses supplying the inner retina. In the macula, three plexuses are situated at different depths. (B) 3D histological images of human retinal vasculature at different eccentricities from optic nerve head. The number of plexuses in the retinal vasculature varies depending on the location of the retina. Both (A) and (B) are from reference [2].

The retinal capillaries and choriocapillaris are major sites for the supply of oxygen and metabolites. While both are essential in the maintenance of the retina, their spatial compositions are distinct. The retinal capillaries have multiple plexuses at different depths. For example, the nerve fiber layer is perfused with its own plexus called retinal nerve fiber layer plexus (RFNLP), which forms radial orientations with the optic nerve head at the center. Embedded in the ganglion cell layer is the superficial capillary plexus (SCP). Between the inner plexiform layer (IPL) and inner nuclear layer (INL) is the intermediate capillary plexus (ICP). The deep capillary plexus (DCP) shows vortex and fern-like shapes and are located in between the INL and the outer plexiform layer (OPL). In the macula, three plexuses SCP, ICP and DCP are well observed, except the foveal avascular zone (FAZ), which has no retinal vasculature. The area between the optic nerve head (ONH) and the macula also contains the RNFLP, totaling four plexuses. In the periphery of the retina, there are two plexuses, with one located above and the other below the inner nuclear layer (INL). In addition to the varying number and shapes of plexuses, these plexuses are interconnected, adding more complexity (Fig. 1.2).

While the retinal capillaries are composed of individual distinct vessel tubes, the choriocapillaris is fenestrated. Situated posterior to the Bruch's membrane as a thin layer, the choriocapillaris also shows different morphologies across the retina. Choriocapillaris forms "honeycomb"-like structures in the fovea, and more "lobular" structures further from the fovea, with lobules increasing in size towards the retinal periphery [3]. The thickness of the choriocapillaris is approximately 10 μm. Beneath the choriocapillaris is the Sattler's layer and Haller's layer, comprised of larger vessels (Fig. 1.3).

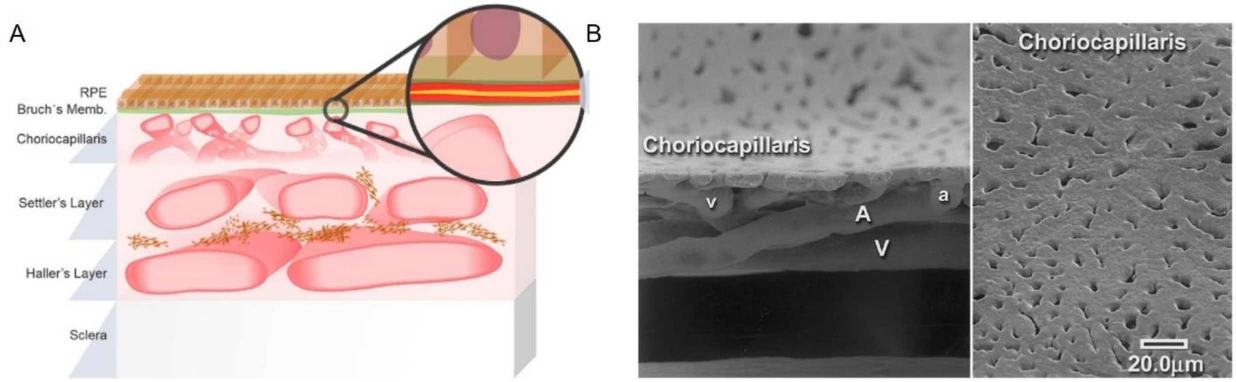

Figure 1.3. Structure of choroidal vasculature and choriocapillaris. (A) Choriocapillaris is the interface between the choroidal vasculature and the outer retina. Beneath the choriocapillaris are Sattler's layer and Haller's layer, with larger vessels. From reference [4]. (B) A choroidal vascular cast of a rat illustrates the spatial arrangement of arterioles and venules below the choriocapillaris (left). Choriocapillaris has a unique fenestrated structure that is different from retina vasculature (right). The arterioles and venules connected to the choriocapillaris are noted 'a' and 'v', respectively. From reference [3].

1.2 Vascular pathology in retinal diseases

Many retinal diseases are vascular in nature and have a vascular component. Neovascularization, characterized by the growth of new blood vessels, is a vascular pathology that can directly impair vision. It manifests in various retinal diseases and can arise from both the retinal and choroidal vasculature. Although the pathogenesis of neovascularization is not fully understood and is likely multifaceted, one possible cause is the abnormal expression of angiogenic factors by retinal tissue, possibly due to ischemia, which stimulates new vessel growth [5, 6]. These new vessels can be more fragile and prone to rupture, leading to leakage. This can result in retinal thickening or cyst formation, or even vitreous hemorrhage, all of which can impair vision [7].

While neovascularization is one of the most extensively studied vascular pathologies in the retina, various vascular lesions are observed even in early stages of diseases. For example, retinal capillaries become non-perfused in eyes with diabetic retinopathy, which can lead to ischemia and further disrupt the remaining retinal vasculature. Similar non-perfusion lesions can also be found in choriocapillaris. In age-related macular degeneration (AMD), both early and advanced stages of the disease have been characterized by the loss and impairment of choriocapillaris using multiple imaging modalities [3]. The relationship between the retinal pigment epithelium (RPE) and choriocapillaris is mutually dependent for normal function, since the RPE's production of VEGF is essential for maintaining the fenestrated structure of the choriocapillaris, while the choriocapillaris provides oxygen and waste removal to the outer retina [8, 9]. Identifying which component initiates the early stages of AMD and the formation of drusen, deposits found under the RPE in AMD, remains an active area of research.

Clinically feasible in vivo detection of retinal/choroidal vasculature disruption will enable early detection of retinal diseases and facilitate risk stratifications. Blood flow speed changes may manifest before the onset of non-perfusion in retinal capillaries or choriocapillaris. Studying these changes could not only deepen our understanding of the role of vasculature in retinal diseases but also identify reversible biomarkers for interventions.

1.3 Optical coherence tomography angiography

Optical coherence tomography (OCT) is an imaging modality routinely used in the ophthalmic clinics [10]. OCT generates depth-resolved cross-sectional images of the retina from the interference pattern between light reflected from the retina and a reference mirror [11]. The depth resolution of OCT makes the modality suitable to study the retina, since the retina has distinctly layered structure and different retinal diseases involve different layers.

In scanning OCT, the most common configuration, a galvanometer scanner scans the beam across the retina, with the center of the pupil as the pivot point. The beam is focused via the cornea and the lens on the retina. The interference pattern from the backscattered light provides the depth profile of the reflectivity at one point on the retina, known as an A-scan. As the beam is scanned in one direction, a cross-sectional 2D image is formed, which is called a B-scan. Moving the beam in the orthogonal direction and compiling B-scans generates a 3D volumetric image of the retina.

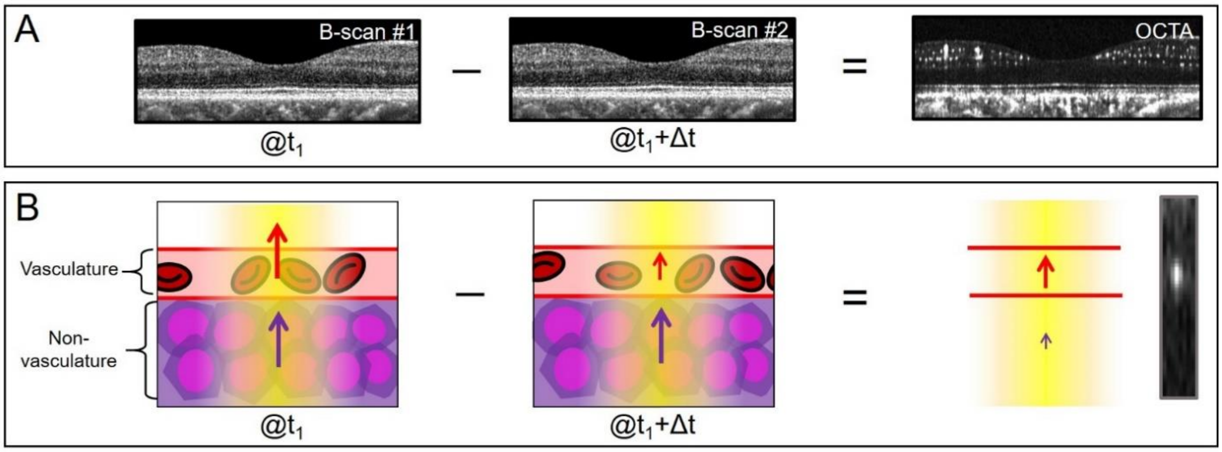

Figure 1.4. Contrast of OCT angiography. (A) The absolute difference between retinal B-scans acquired with a time gap (interscan time, Δt) visualizes the retinal vasculature (right). Small dots in the inner retina in the OCTA B-scan correspond to cross-sections of capillaries. (B) The principle of OCTA. The red blood cells move during the interscan scan time and generate temporal fluctuations of OCT signal, which can be visualized by comparing the B-scans.

OCT angiography (OCTA) is an extension of OCT, which visualizes both retinal and choroidal vasculature [12-14]. To generate OCTA, repeated B-scans are acquired from the same location. The contrast in OCTA comes from the changes in OCT intensity over time, resulting from red blood cell displacement during the repeated scans. Unlike vessels, static tissues such as neural tissues maintain consistent intensity profiles over repeated scans. These temporal fluctuations in B-scans are used to generate contrast for the vasculature (Fig. 1.4). Since an OCTA protocol is simply an OCT protocol with repeated B-scans, it requires minimum hardware changes for implementation and maintains the key advantages of OCT, such as non-invasiveness and depth resolution. Moreover, since OCTA is co-registered with OCT scans, it simultaneously achieves structural and vascular imaging of the retina.

However, OCTA faces various challenges. Since the contrast is derived from fluctuations in OCT B-scans, patient movements or changes in fixation can result in high OCTA signals unrelated to the vasculature. Additionally, the need for repeated B-scans leads to increased imaging time. Another major challenge arises from the common practice of evaluating angiograms in an en face view rather than a cross-sectional view. This necessitates isotropic scanning in both the B-scan direction and its orthogonal direction, which are often referred as ‘fast’ and ‘slow’ scan direction, respectively. In contrast to retinal structural imaging, where B-scan spacings are often set wider than the A-scan spacing based on the size of the biomarker of interest, the requirement for en face angiograms calls for isotropic scanning, which significantly increases imaging time.

Projection artifacts are another major challenge in OCTA [15, 16]. Since OCT beam reaching the deeper tissue goes through the superficial tissue double-pass, the fluctuation in the superficial tissue also generates the fluctuation in the deeper tissue OCT signal. Also, the forward scatterings in vessels before the back scattering also manifests as the optical path length elongation; since the forward scatterings are temporally dynamic, it also generates contrast in OCTA outside the vessels. This results in vessels showing ‘tails’ along the beam direction, known as shadow or projection artifacts. Therefore, superficial vessels are consistently observed in the deeper tissues. This can present a challenge in imaging the deep capillary plexus, or choroidal vasculature, both of which are positioned posterior to the superficial vessels in the retinal vasculature, including arterioles and venules.

Lastly, OCTA is a structural imaging of the vasculature, and therefore provides limited information about hemodynamic such as blood flow or its speed. OCTA in its current form, which provides information about ‘vessel’ or ‘non-vessel’, has been extensively studied to characterize many retinal diseases. While decorrelation of OCT and OCTA and their relationships with flow speed have been extensively characterized in vitro, blood flow speed quantification in human retina has been limited. Blood flow speed imaging from OCTA may enable i) detecting the irregular blood flow speed in the vasculature before complete non-perfusion of retinal capillaries or loss of choriocapillaris, and ii) detecting flow speed characteristics associated with new vessel growth before the onset of the neovascularization. These advancements could facilitate our understanding of the role of vasculature in retinal diseases, improve patient risk stratification, and also provide target biomarkers that can be reversed.

1.4 Aim of the thesis

In this thesis, a method to quantify retinal blood flow speed using OCTA protocols is presented, named the second-generation variable interscan time analysis (2^{nd}-gen VISTA). The total acquisition time is under 4 seconds and the field-of-view is up to 5 mm x 5 mm, which spans the majority of the macula. The method adopts a simple exponential decay model for temporal autocorrelation $\rho(t) = \exp(-\alpha\tau)$, and evaluates the temporal autocorrelation decay constant (α) at the individual capillary level as a surrogate marker for blood flow speed. This is enabled by high

A-scan rate swept-sources which provides short interscan times and fine A-scan spacing. The blood flow speed modulation from the cardiac pulsatility can be extracted from the proposed method, and a pulsatility compensation method is proposed. Projection artifacts are suppressed using a curvilinear structure detector which leverages the planar shape of the artifacts. The new OCTA blood flow speed quantification shows different blood flow speed markers in different capillary plexuses, and the correspondence between the lobular structures of choriocapillaris and the pattern of high α regions. Pseudo colormap provides information about α, and eyes with diabetic retinopathy and AMD have been imaged. The repeatability of α and the compatibility of α measurements from different OCTA protocols are also evaluated.

Chapter 2

High A-scan rate OCTA and retinal blood flow speed quantification

2.1 Blood flow speed measurements using ophthalmic imaging modalities

2.1.1 Doppler OCT

Doppler OCT is an extension of OCT that utilizes Doppler effect to measure the blood flow velocity in the retina [17]. Doppler OCT acquires A-scans with overlaps to evaluate the phase between the A-scans caused by red blood cells moving toward or away from the beam direction. Doppler OCT can differentiate the direction of the blood flow, and the conversion from phase changes to actual velocity is straightforward. A volumetric Doppler OCT scan of the optic nerve head allows for the calculation of total retinal blood flow [18].

Doppler OCT can only detect the movements that are parallel to the beam detection. Since the arteries and veins are in axial orientation at the ONH, Doppler OCT can be readily applied. Outside the ONH, however, vessels tend to be parallel to the retina and thus orthogonal to the OCT beam direction, especially in the macula. Capillary plexuses, such as the deep capillary plexus (DCP) situated between the inner nuclear layer (INL) and the outer plexiform layer (OPL), also align along the retinal layers, making them orthogonal to the OCT beam. Additionally, Doppler OCT requires knowledge of the angle between the vessel and the beam for blood flow speed calculation. However, Doppler OCT alone does not readily resolve capillaries, posing a challenge in acquiring the necessary structural information of the vasculature to determine these angles.

2.1.2 OCT angiography (OCTA)

Unlike Doppler OCT, where the focus is on measuring blood flow speed in vessels that are parallel with respect to OCT beam, OCT angiography (OCTA) adopts an approach that the contrast is from decorrelation between repeated imaging. Therefore, OCTA can highlight vessels regardless of their orientations.

OCTA is commercially available and has been extensively used to study retinal vascular lesions [14, 19]. In retinal vasculature, OCTA non-invasively visualizes capillary drop-out, neovascularization and microaneurysms[20-22]. Vessel densities, evaluated from skeletonized vessels, have been studied in diabetic retinopathy, including their association with the severity of the disease [23, 24]. Recent advancements in wide-field OCTA have enabled the study of non-perfusion in the retinal periphery in diabetic retinopathy [25]. The depth resolution of OCTA has facilitated the detection of intraretinal microvascular abnormality (IRMA) and enabled studies on the locations of microaneurysms [26-28]. Furthermore, the different plexuses were studied separately, and the vulnerability of the DCP has been suggested in diabetes and early DR. OCTA also readily visualizes the radial peripapillary capillary plexus (RPCP), the capillary plexus surrounding the ONH with a radial orientation, and has been used to characterize glaucoma [29].

In choroidal vasculature, OCTA has visualized the choriocapillaris and type 1 macular neovascularization (MNV) in age-related macular degeneration (AMD), where new vessels form in the choroidal vasculature, posterior to the RPE. Type 1 MNV shows features distinct from normal choriocapillaris, and its presence has been linked to an increased risk of developing wet AMD [30]. Additionally, choriocapillaris flow deficits, an OCTA biomarker in choriocapillaris that is analogous to non-perfusion in retinal vasculature, has been associated with the progress of geographic atrophy [31].

While OCTA has enabled clinical studies on the retinal and choroidal vasculature, OCTA in its traditional form only provides contrast for the vasculature structure, but not the information about the blood flow speed.

In vitro studies, utilizing M-mode acquisitions, have demonstrated that OCTA signal intensity increases with longer interscan times until it reaches saturation [32-35]. This phenomenon is well expected, as OCTA contrast is derived from the decorrelation caused by the movement of scatterers, such as red blood cells. The OCTA signal saturates when the scatterer displacement becomes comparable to the transverse point spread function of the OCT beam. Notably, faster blood flow speeds result in quicker saturation of the OCTA signal. This is because a higher flow speed leads to a larger displacement of scatterers, reaching the point of complete decorrelation and

OCTA saturation, in a shorter interscan time. This relationship between blood flow speed and OCTA signal saturation is illustrated in Figure 2.1.

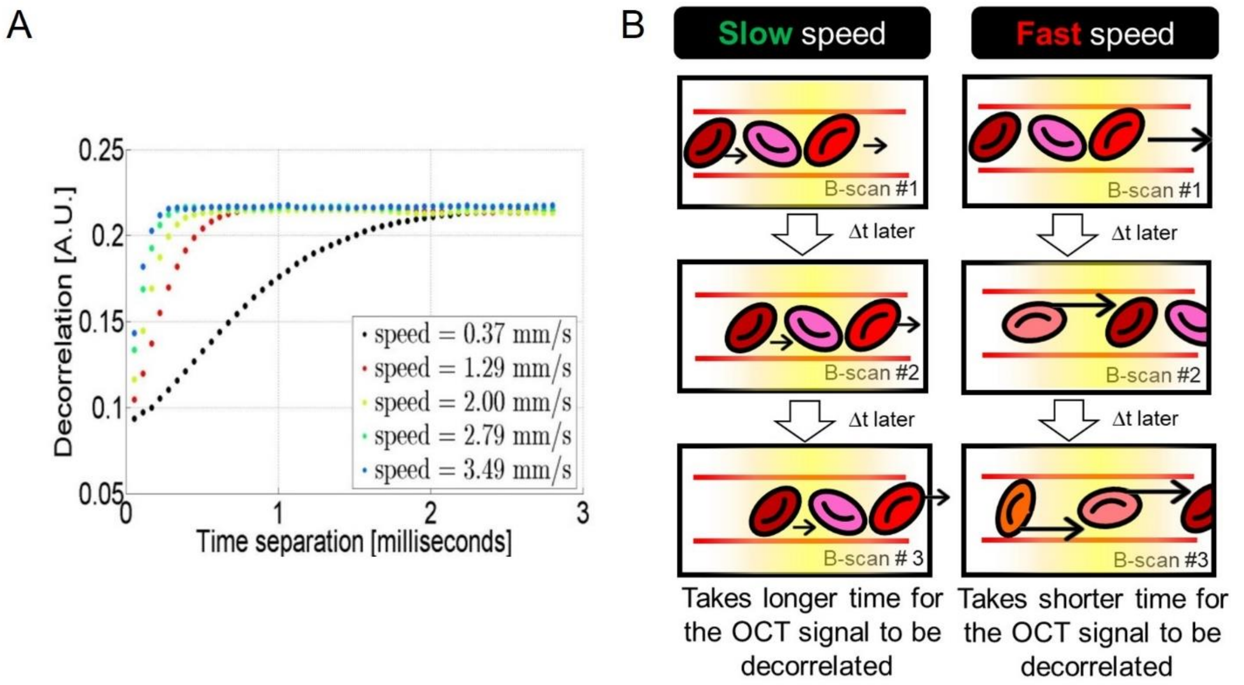

Figure 2.1. Blood flow speed and OCTA saturation/temporal autocorrelation decay. (A) Higher blood flow speed leads to a more rapid saturation of OCTA. The graph is from reference [35], which adopted M-mode acquisitions on human blood in a glass tube. (B) Displacement of red blood cells during interscan times cause decorrelation in OCT signal. If the blood flow speed is slow (left), the time it takes for decorrelation is longer; it the speed is fast (right), OCT signal decorrelates rapidly. The width of the beam (yellow, at the middle of each B-scan) will change the speed of decorrelation.

Therefore, OCTA at multiple interscan times can be used to characterize the decay of temporal autocorrelation and extract a marker for retinal blood flow speeds. This assumes that OCTA signal is not fully saturated at the shortest interscan time. OCTA at various time points can be acquired by multiple B-scan acquisitions (more than two). Multiple B-scan acquisitions (>2) enabled acquisition of OCTA at multiple time points. This approach was first developed by Choi et al. and Ploner et al., and named variable interscan time analysis (VISTA) [36, 37]. In the original VISTA method, a dimensionless metric termed ‘relative blood flow speed’ was employed. This metric is the ratio between OCTA values at two interscan times (1.5 ms and 3 ms). For fast blood flow speeds, the OCTA values at these two time points would be similar, as the OCTA signal would already be fully saturated at the shortest interscan time, resulting in a ratio close to 1. Conversely, with slower blood flow speeds, the OCTA signal would not be fully saturated, leading to a ratio less than 1. This relative blood flow speed was then mapped to the hue in the HSV colormap to generate a false-colored enface image. The original VISTA has been used to qualitatively characterize eyes with diabetic retinopathy, polypoidal choroidal vasculopathy and age-related macular degeneration [38-40].

The original VISTA demonstrated the potential of high-speed OCTA to provide insights into blood flow speed. However, its dimensionless metric lacked a clear connection to the in vitro OCT temporal autocorrelation studies. Additionally, the method compared OCTA values at the pixel level from two time points in en face images, both subject to stochasticity. This often resulted in a significant portion of en face pixels with the ratios exceeding 1, necessitating an artificial cap. Furthermore, the approach employed a joint bilateral filter on the final relative blood flow speed metric, using OCTA values for the range kernel. This implicitly assumed that similar OCTA values corresponded to similar blood flow speeds, which may not always hold true.

2.1.3 Adaptive optics and feasibility of blood flow speed quantification in retinal capillaries using non-AO OCTA

Adaptive-optics (AO) retinal imaging has been essential in understanding the blood flow speed in the retina [41]. AO provides an exceptional transverse resolution, achieved by aberration correction using wavefront shaping. While AO provides a limited filed-of-view and lacks intrinsic depth resolution, its fine transverse resolution enables identification of individual red blood cells. Therefore, AO allows for direct measurement for blood flow speed. This technology has been instrumental in enhancing our understanding of the range of blood flow speeds, the nature of pulsatility and its propagation, variations in speed, and responses to stimulation in retinal capillaries (Fig. 2.2) [42-47].

In contrast, non-AO OCT, due to its limited transverse resolution, requires indirect methods for characterizing blood flow speed, such as using surrogate markers like temporal autocorrelation. The range of blood flow speeds reported in adaptive optics studies, typically around 1 mm/s and generally not exceeding 3 mm/s even at maximum from pulsatility, suggests that a high A-scan rate non-AO OCTA can effectively evaluate temporal autocorrelation decay by measuring OCTA before its full saturation. For example, a 1.4 mm $1/e^2$ diameter at the pupil with 1050 nm wavelength would result in 16 μm $1/e^2$ diameter (10 μm FWHM) when focused with a 17 mm focal length lens. The optical aberrations and longer axial eye length would make the actual transverse point spread function on the retina larger, but this provides a conservative estimation on the types of vessels whose blood flow speed can be characterized using OCTA. Assuming ~1 ms shortest interscan time, the displacement of red blood cell in capillaries would be smaller than the transverse PSF, indicating the OCTA saturation can be captured with multiple interscan times OCTA. However, in large vessels with diameter >40 μm, the blood flow speed has been reported to be >10 mm/s. In this case, the displacement even at the shortest interscan time is enough to cause complete decorrelation and the suggested ~ 1 ms shortest interscan time OCTA protocols would not capture the OCTA saturation. Recent developments in MEMS-VCSEL technology has realized high A-scan rate OCT ranging from 200 kHz to multi-MHz [48-50]. This allows for OCTA with short interscan times, fine A-scan spacing to resolve capillaries, and clinically feasible total acquisition time without eye tracking.

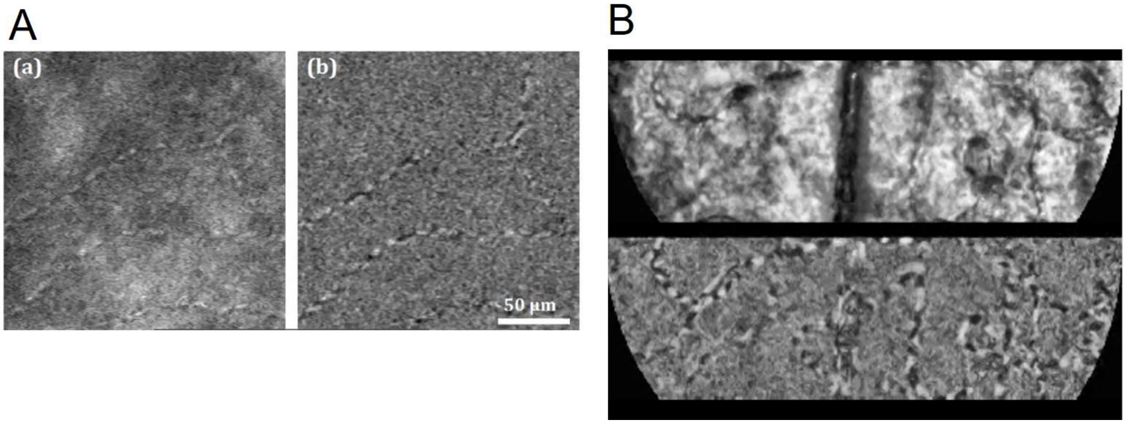

Figure 2.2 Adaptive optics in human retina. Adaptive optics scanning laser ophthalmoscope (AO-SLO) provides a transverse resolution that enables identification and tracking of individual red blood cells. (A): Capillaries near the foveal avascular zone imaged with AO-SLO detecting multiply scatter light (left). The right panel emphasizes the moving red blood cells. The image is from reference [44]. (B): The top panel shows an AO-SLO image of retinal capillaries captured at 400 frames-per-second. A temporal filtering emphasizes moving red blood cells. (bottom panel). The image is from reference [46].

2.2 Participants

Only healthy normal subjects were imaged at Massachusetts Institute of Technology. Healthy normal subjects and patients with retinal diseases were imaged at the New England Eye Center of Tufts Medical Center. Prior to imaging, written informed consent was acquired. The study was approved by Massachusetts Institute of Technology Committee on the Use of Humans as

Experimental Subjects and Tufts Medical Center Institutional Review Boards. Written informed consent was obtained before imaging.

2.3 Swept-source OCT/OCTA

2.3.1 Swept-source OCT schematics

A 600 kHz A-scan rate retinal SS-OCT system was developed using a custom micro-electromechanical systems vertical cavity surface emitting laser (MEMS-VCSEL). The center wavelength was 1050 nm and the sweep bandwidth was ~100 nm. The MEMS-VCSEL controls the output wavelength by changing the voltage between the suspended mirror and the substrate mirror. The voltage signal was optimized to linearize the wavenumber sweep across the time to ensure uniform SNR over the sweep when the sample rate is fixed. OCT schematics are shown in Figure 2.3.

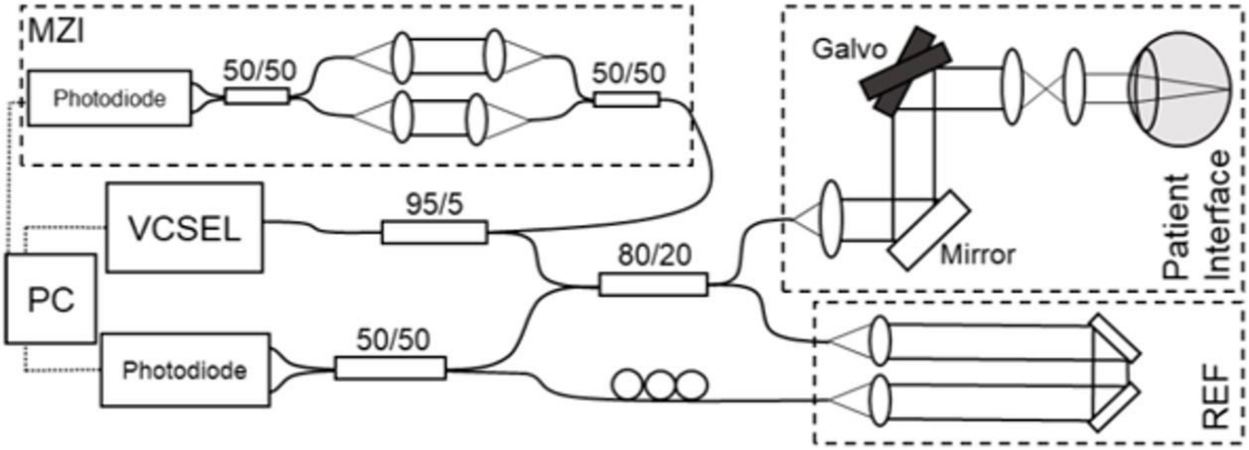

Figure 2.3. Schematics of the 600 kHz prototype swept-source OCT system.

Mach Zehnder interferometer signal was sampled simultaneously using balanced photodetectors and a 12 -bit digitizer (ATS9373, Alazar). The sample rate was at 2 GS/s. MZI signal was used to compensate sweep-to-sweep variation of the laser source. Hilbert transform was applied on MZI signal to generate the phase evolution over time. The temporal points corresponding to uniform phase steps were calculated. Then, the corresponding OCT signal was interpolated at these points.

A galvanometer (6210 H, Cambridge Technology) was used to scan the retina. The saw-tooth pattern was used with the scan duty cycle near 75%. At the pupil, $1/e^2$ diameter of the beam was

1.4 mm. Refractive error of the eye was corrected without translating the OCT optics; an electrically focus tunable liquid lens (EL-10-30-C-NIR-LD-MV, Optotune) was placed in a vertical orientation before the galvanometer.

During the image acquisition, the subject was aligned using an iris camera. The ocular lens had four red light-emitting diode (LED) lights, which were reflected at the eye. The LED lights were used for a primary alignment between the OCT system and the subject. Once the retina was captured in the preview, a manual joystick and a vertical linear stage were used for fine alignment. Then, the liquid lens was controlled based on the intensity of the preview. In the preview display, where OCT cross-sectional views were presented in a logarithmic scale, the intensity of hypo-reflective retinal layers such as INL and ONL were used to determine the optimal focus. Subjects were instructed to fixate on a cross fixation target which was shown using a beam projector and neutral density filters. Figure 2.4 shows the deployed SS-OCT system.

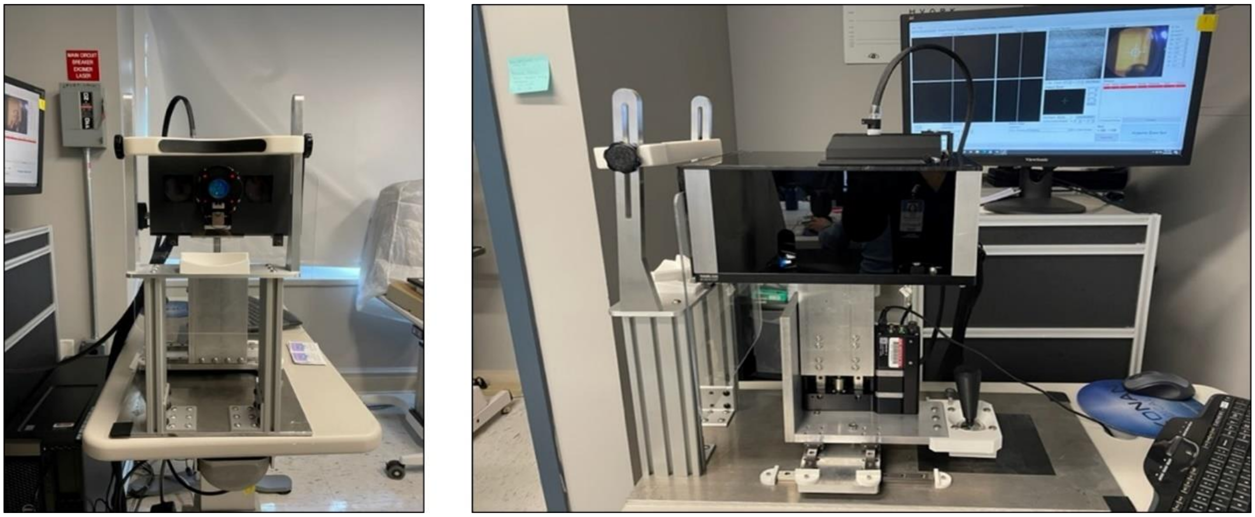

Figure 2.4. Swept-source OCT system deployed at the New England Eye Center. Left: front view. Right: side view.

2.3.2 OCTA protocols and its reconstruction

Here, the fundamental interscan time Δt is the interscan time of subsequent B-scans. If a protocol acquires N B-scan repeats, OCTA at N – 1 different interscan times can be calculated. For example, 2 Δt interscan time OCTA will compare every other B-scans and (N-1) Δt interscan time OCTA will compare the first and the last B-scan (Fig. 2.5). The following formula was used to generate unnormalized and normalized OCTA. Here L is the number of split spectra, and three Gaussian bands with the adjacent bands crossing each other at 64% of the peaks were used, which better matches axial and transverse resolution [13]. S^{i}_{j} is the j^{th} repeated OCT B-scan from the i^{th} spectrum.

$$\begin{aligned}\text{OCTA}_{\text{unnormalized}}(M\Delta t) &= \frac{1}{L(N-M)}\sum_{i=1}^{L}\sum_{j=1}^{N-M}|S^{i}{}_{j+M}-S^{i}{}_{j}\,| \\ \text{OCTA}_{\text{normalized}}(M\Delta t) &= \frac{1}{L(N-M)}\sum_{i=1}^{L}\sum_{j=1}^{N-M}\frac{(S^{i}{}_{j+M}-S^{i}{}_{j})^{2}}{(S^{i}{}_{j+M})^{2}+(S^{i}{}_{j})^{2}}\end{aligned} \tag{Eq. 2-1}$$

It is worth to note that unnormalized OCTA and normalized OCTA are appropriate for different applications. In the retina, where transparency of the inner retina facilitates more light reaching to photoreceptors, vessels and red blood cells are more scattering (hyper-reflective) compared to the non-vasculature tissue. Therefore, retinal capillaries are readily observed in the structural OCT alone, especially ICP and DCP since the INL that both plexuses are bordering is hypo-reflective. Therefore, in the retina, unnormalized OCTA can be useful in generating the structure of the vasculature. However, note that this is specific to the inner retina where static tissues are hypo-scattering. In the outer retina, the bands are hyper reflective and therefore adopting unnormalized OCTA generates high OCTA signal. This should be excluded using proper layer segmentation. Furthermore, in sclera, the vasculature is not relatively more scattering than its surrounding tissue.

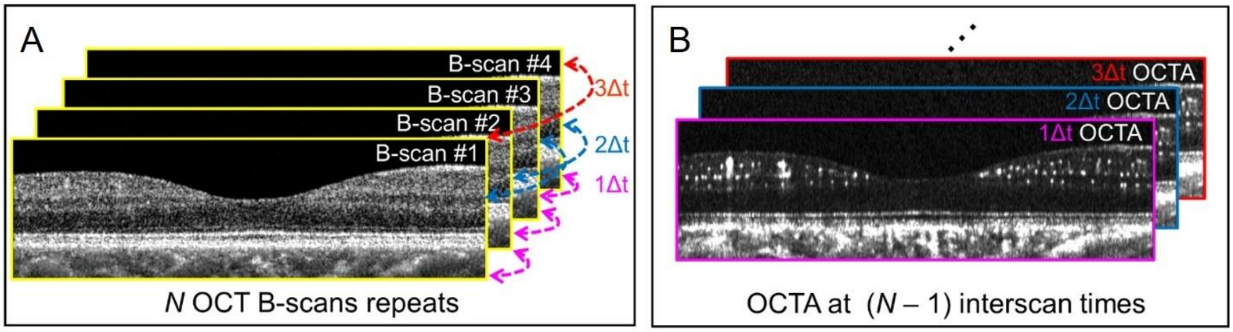

Figure 2.5. Multiple OCT B-scan repeats provide OCTA measurements at various interscan times

Normalized OCTA, however, contains a direct measurement of decorrelation where temporal autocorrelation model can be used to evaluate blood flow or its speed. Hypo-reflective tissues can give rise to high normalized OCTA values, since the ratio of the noise to their base intensity is higher. Conversely, normalized OCTA values from hyper reflective structure, such as well segmented vessels, choriocapillaris, and outer retina is less likely to be generated by noise. When the SNR is high enough, normalized OCTA is also more robust against to illumination artifacts than unnormalized OCTA. Adopted OCTA protocols are summarized in Table 2.1.

FOV	Fundamental interscan time	A-scan spacing	B-scan repeats	Scanner duty cycle	A-scans / B-scan	B-scans	Acquisition time
3 mm × 3 mm	1 ms	6.7 µm	8	0.75	450	450	3.60 s
5 mm × 5 mm	1.25 ms	8.8 µm	5	0.76	570	570	3.57 s

Table 2.1. OCTA protocols

2.3.3 Inter B-scan registration

The unnormalized OCTA B-scan was registered to the OCTA B-scan in the previous position to compensate the motion and eye movements. Only rigid translation at integer pixel was used, therefore this did not compensate for tilt and subpixel motions [51]. Nevertheless, this inter B-scan registration, which leveraged the sparsity of retinal vasculature, improved the connectivity of vessels. It also enabled OCT layer segmentation at the whole volume level, not individually from B-scans, making the segmentation robust and more isotropic over fast-scan and slow-scan direction.

2.3.4 Retinal layer segmentation and manual correction

Retinal layer segmentation is crucial both for retinal and choroidal vasculature. Since retinal vasculature has multiple plexuses compartmentalized according to the retinal layers, studying different plexuses requires corresponding layer segmentation. En face angiogram without the segmentation of the outer retina using unnormalized OCTA would make resolving retinal capillaries challenging. Choriocapillaris is a thin layer located posterior to the Bruch’s membrane, with 8 ~ 10 µm of thickness. Therefore, Bruch’s membrane segmentation needs to be consistent to correctly segment the choriocapillaris layer across the field-of-view.

From the inter B-scan registered volume, the RPE was segmented for each B-scan, which was smoothed across the volume using 2D local regression smoothing (MATLAB fit function with ‘lowess’ option, with ‘Span’ corresponding to 500 µm × 500 µm). The RPE segmentation was then used for flattening the volume. To segment further inner retinal layers, the RPE flattened volume was smoothed using a 3D Gaussian filter. Then, the internal limiting membrane, posterior of retinal nerve fiber layer and the middle of inner nuclear layer was segmented using simple peak detection and thresholding. Then the segmentation results were manually inspected and corrected. Rough guidance provided by a reader was used to find the local maximum of "feature" specific to each layer. The intensity increase along the axial direction was used for ILM, intensity decrease along axial direction for RNFLP and the low intensity for the middle of INL. These manually corrected segmentations were smoothed using the same local regression smoothing algorithm used for the RPE. The 'Span' option was 150 µm × 150 µm and 300 µm × 300 µm for ILM and the middle of INL, respectively. The RNFL thickness was smoothed with 1000 µm × 1000 µm span option, which was then used to locate the RNFLP. Note that the 'Span' option is layer specific, but also it could be disease specific.

The three segmented inner retinal layers compartmentalized the retinal vasculature into three categories: RNFL plexus (RNFLP), superficial capillary plexus + intermediate capillary plexus (SCP + ICP) and deep capillary plexus (DCP). For the RNFLP region, the region between 19 µm posterior to the ILM and posterior to the RNFL was used. The 19 µm posterior shift from the ILM excluded regions with specular reflections of OCT beam. Also RNFLP thinner than 19 µm has been reported to be avascular [52]. The SCP + ICP region was between the posterior of the RNFL and middle of the INL. The DCP region was between the middle of the INL and 80 µm anterior to the RPE.

For the choriocapillaris identification, consistent segmentation of the RPE is crucial. As a fine tuning for the RPE segmentation, the posterior local intensity peak in Bruch's membrane-RPE complex was detected from the RPE flattened volume, which was Gaussian filtered only in the transverse direction. The median filter with a window size of 200 µm × 200 µm was used to smooth the segmentation and used for the choriocapillaris slab segmentation; the middle of the slab was 13 µm posterior to the segmented posterior local intensity peak, with a 8 µm thickness.

2.4 Blood flow speed quantification in the retina

2.4.1 Temporal autocorrelation decay and OCTA

OCT signal from a voxel at x at time t can be separated into static and dynamic components, $S(x, t) = S_{static}(x) + S_{dynamic}(x, t)$, where the expected value of $S_{dynamic}$, $E[S_{dynamic}]$, is zero. In the retinal vasculature, $S_{dynamic}$ arises from moving red blood cells, assuming negligible patient movement. Note that this does not treat the red blood cells as point scatters or assume the shape of the OCT beam. Over a period significantly shorter than the cardiac cycle, S(x, t) can be treated as a wide-sense stationary process; the cardiac pulsatility can modulate blood flow speed more than two times. We define a metric A(τ), as the scaled ratio of following quantities: i) the squared difference of OCT acquired with interscan time τ and ii) the expected value of the square of the OCT signal [53]. The numerator is $E[|S(x, t + \tau)-S(x, t)|^2] = 2(\mathrm{Var}[S_{dynamic}] – R_{dynamic}(\tau))$, where $R_{dynamic}(\tau)$ is the autocorrelation function of $S_{dynamic}(x, t)$. The denominator is $E[|S(x, t)|^2] = |S_{static}|^2 + \mathrm{Var}[S_{dynamic}]$. Since $E[S_{dynamic}]$ is set zero, $\mathrm{Var}[S_{dynamic}]$ equals $R_{dynamic}(\tau = 0)$. With the scale factor ½,

$$A(\tau) = \frac{1}{2}\frac{E[|S(x,t+\tau) - S(x,t)|^2}{E[|S(x,t)|^2]} = \frac{\mathrm{Var}\left[S_{dynamic}\right] - R_{dynamic}(\tau)}{|S_{static}|^2 + \mathrm{Var}\left[S_{dyanmic}\right]}$$

$$= \frac{Var\left[S_{dyanmic}\right]}{|S_{static}|^2 + Var\left[S_{dyanmic}\right]}\left(1 - \frac{R_{dyanmic}(\tau)}{R_{dyanmic}(\tau = 0)}\right) = \beta\left(1 - \rho(\tau)\right) \qquad \text{Eq. 2-2}$$

$\beta = \mathrm{Var}[S_{dynamic}]/(|S_{static}|^2 + \mathrm{Var}[S_{dynamic}])$ models the ratio of dynamic versus static contribution to the signal, and $\rho(\tau) = R_{dynamic}(\tau)/R_{dynamic}(\tau = 0)$ models the normalized autocorrelation (autocorrelation coefficient) decay of the dynamic signal. The portion of the dynamic signal contribution is modeled by β and not ρ(τ). As shown in Figure 2.1, the fast blood flow speed will lead to a rapid autocorrelation decay, and the slow blood flow speed will cause a slow autocorrelation decay. OCTA normalized formula in Eq. (2.1) is sampling the ratio of squared difference of the OCT signal to the sum of square of the OCT signal at two time points. Therefore, $OCTA_{normalized}$ can be treated as sampling of A(τ) at discrete interscan times $\tau = \Delta t, 2\Delta t, \dots (N – 1)\Delta t$, in which case β is the saturated value of the $OCTA_{normalized}$.

With M-mode, various types of temporal autocorrelation functions, ρ(τ), in OCT have been suggested to characterize fluid dynamics of scatterers. Notably, Wang et al. approximated the amplitude of backscattered light as a sequence of square pulses and modeled autocorrelation function as $\rho(\tau) = 1 - \alpha'\tau$ when τ is small [33]. The authors experimentally validated a linear relationship between α' and the transverse velocity using intralipid particles. Tokayer et al. demonstrated a linear relationship between normalized OCTA and particle speeds when the interscan time is small, using human whole blood flowing in a glass tube [35]. The time range where the linear relationship held was dependent on the blood flow speeds (e.g. <0.3 ms for 1.5

mm/s blood flow speed). 1.5 mm/s is in the range of retinal capillary blood flow speeds and 0.3 ms is significantly smaller than the shortest interscan time achievable with a galvanometer scanner. Note that the linear relationship between OCTA and the interscan time from Tokayer et al. is consistent with Wang et al.'s results, both of which assume the interscan time is small. Lee et al. proposed a dynamic light scattering OCT which comprehensively modeled the static and noise component of complex OCT signal [32]. The authors treated diffusion and translational movement of particles separately. The diffusion decayed the autocorrelation according to $\exp(-\alpha_1\tau)$ and the translational movement to $\exp(-\alpha_2\tau^2)$. However, Lee et al. assumed point scatterers, which does not model retinal OCT beam and red blood cell, since red blood cell is smaller, yet comparable to the point spread function. Furthermore, red blood cell movement in capillaries is fixed and there is no diffusion. Recently, Nam et al. modeled the autocorrelation as $\rho(\tau) = \exp(-\alpha\tau^2)$ and measured pulsatility in large vessels in human retina [34].

Temporal autocorrelation studies above have adopted M-mode scan, where one point is repeatedly imaged before imaging the next point. Each point is sampled for 100 times or more, providing large sampling and fine temporal points (<100 μs). However, in OCTA, the shortest interscan time achievable with a galvanometer scanner is inertia limited, often around 1 ms. Also, the total acquisition time is limited, therefore >100 repeated sampling is unfeasible in a clinical setting. For example, even with a 1 MHz A-scan rate, imaging 5 x 5 mm with 10 μm spacing (required for capillary resolution) with 100 repeat A-scan will require 25 seconds acquisition time.

2.4.2 OCTA protocols for clinical feasibility and an exponential decay model for temporal autocorrelation

For blood flow speed quantification OCTA protocols to be clinically feasible, it should provide multi mm^2 field-of-view, fine A-scan spacing enough to resolve capillaries, multi B-scan repeats to characterize OCTA saturation, and short total imaging acquisition time. When the total acquisition time is over 4 seconds, eye blinking of subjects is virtually unavoidable, therefore blink detections and eye tracking are needed. Blinking also introduces the discontinuity of cardiac pulsatility, which can be problematic in pulsatility compensation. Since hundreds of A-scans are needed for each B-scan, necessitated by the FOV and fine A-scan spacing requirement, the number of B-scan repeats has to be <10. These OCTA protocol requirements limited our choice of temporal autocorrelation function. Even the shortest interscan time of ~1 ms, which is set by the inertia limit, was too long for a linear model. The number of temporal points for $\rho(\tau)$ fitting is limited by both i) the number of B-scan repeat requirement (<10) for total acquisition time, and ii) interscan time >10 ms would produce fully saturated OCTA even in capillaries (1 mm/s *10 ms ≈ FWHM of the transverse point function). Therefore, complex models with multiple parameters may lead to overfitting. Here, $\rho(\tau) = \exp(-\alpha\tau)$ was adopted due to its simplicity and the ease of interpretation of α as temporal autocorrelation decay constant. When the interscan time is small, $\rho(\tau)$ approximates the linear relationship reported from Tokayer et al., since $\mathrm{OCTA}_{\mathrm{normalized}} = \beta(1-\exp(-\alpha\tau)) \approx \beta\alpha\tau$ when $\alpha\tau \ll 1$. While other simple autocorrelation models could be possible, the models need to present both i) linear relationship when τ is small and ii) saturation when τ is large.

2.4.3 Spatial compilation tactics

In retinal capillaries, while red blood cells mostly form single files, blood flow is still stochastic. Therefore, to robustly characterize autocorrelation decay, a large number of samples that measure decorrelation (e.g. OCTA) are necessary. In M-mode acquisitions, this large sampling requirement is readily achieved with >100 repeated A-scans and temporal resolution of <100 µs. However, with multi mm^2 FOV OCTA protocols, the number of sampling at each position is <10 and temporal resolution is limited at ~1 ms due to the inertia of the galvanometer. Here, the large number of samples was achieved by spatial compilation of OCTA measurements over a spatial domain in which blood flow speeds are expected to be uniform, instead of >100 repeated measurement.

Note that there is an inherent trade-off between the spatial resolution of blood flow speed quantification and the SNR of OCTA signals compiled for autocorrelation decay. For retinal vasculature, AO studies have shown that the blood flow speeds in capillaries can change significantly (>2×) at bifurcation points [45, 46], making individual capillary segments the largest spatial domain where uniform blood flow speeds can be assumed. Therefore, we spatially compile OCTA measurements over each capillary segment and evaluate a temporal autocorrelation decay constant for individual capillary segments.

2.4.4 OCTA projection artifacts and Optimally Oriented Flux

For correct spatial compilation, a 3D retinal vessel mask is needed, which contains only voxels that are part of the vasculature. Compiling OCTA measurements from the non-vessel and vessel would lead to an underestimation of autocorrelation decay. A simple thresholding on OCTA cannot be used since projection artifacts would be classified as vessel voxels. Therefore, a 3D vesselness detector that can exclude projection artifacts and only keep real vessel is needed.

Here, Optimally Oriented Flux (OOF) was applied on unnormalized retinal OCTA [54]. OOF is a curvilinear structure detector that quantifies the image gradient sum across the surface of a sphere along three orthogonal directions, represented with three eigenvalues. For example, a planar structure has one large negative eigenvalue with its corresponding direction normal to the plane, and two small eigenvalues with two directions parallel to the plane, assuming the target radius is close to the half of the thickness of the plane. A tubular structure has two large negative eigenvalues with directions normal to the tube axis, and one small eigen value along the tube axis. While the Hessian matrix, a commonly used curvilinear structure detector, considers both the intensity inside and outside the sphere, OOF uses only the local image gradient at the sphere surface. Therefore, OOF can detect target shapes even when surrounded by other features. This robustness makes OOF particularly suitable for acquiring a 3D retinal vessel mask without projection artifacts, since retinal capillaries are closely situated and projection artifacts extend directly from their origin vessels. The OOF vesselness response proposed by Law and Chung was used with unnormalized OCTA as input [54]. The radius of the OOF response was set to twice the A-scan spacing to avoid identifying noise as vessels. Note that diameters of human retinal capillaries are smaller than the expected transverse point spread function of OCT.

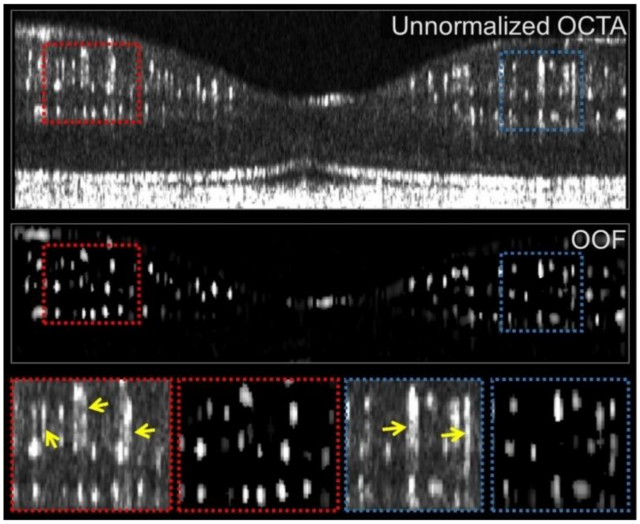

Figure 2.6. Unnormalized OCTA and Optimally Oriented Flux (OOF). OOF application on unnormalized OCTA suppresses projection artifacts. Two ROIs are selected and magnified in the

bottom row. Yellow arrows denote projection artifacts in the original unnormalized OCTA that are suppressed in the OOF.

Since projection artifacts have shapes of the origin vessel that is shadowed along the beam direction, the OOF response from the projection artifacts has a large λ_1 along the transverse direction normal to the tube axis, but a small λ_2 along the axial direction. However, real vessels have large λ_1 and λ_2. Therefore, adopting the $(\lambda_1\lambda_2)^{1/2}$ suppresses projection artifacts and highlights real vessels. Figure 2.6 shows that the OOF response maintains inter-plexus connections and show three distinct plexuses in the cross-sectional view. To generate a 3D vessel mask, the Otsu threshold was applied on the logarithm of the OOF response as the global threshold (Fig. 2.7).

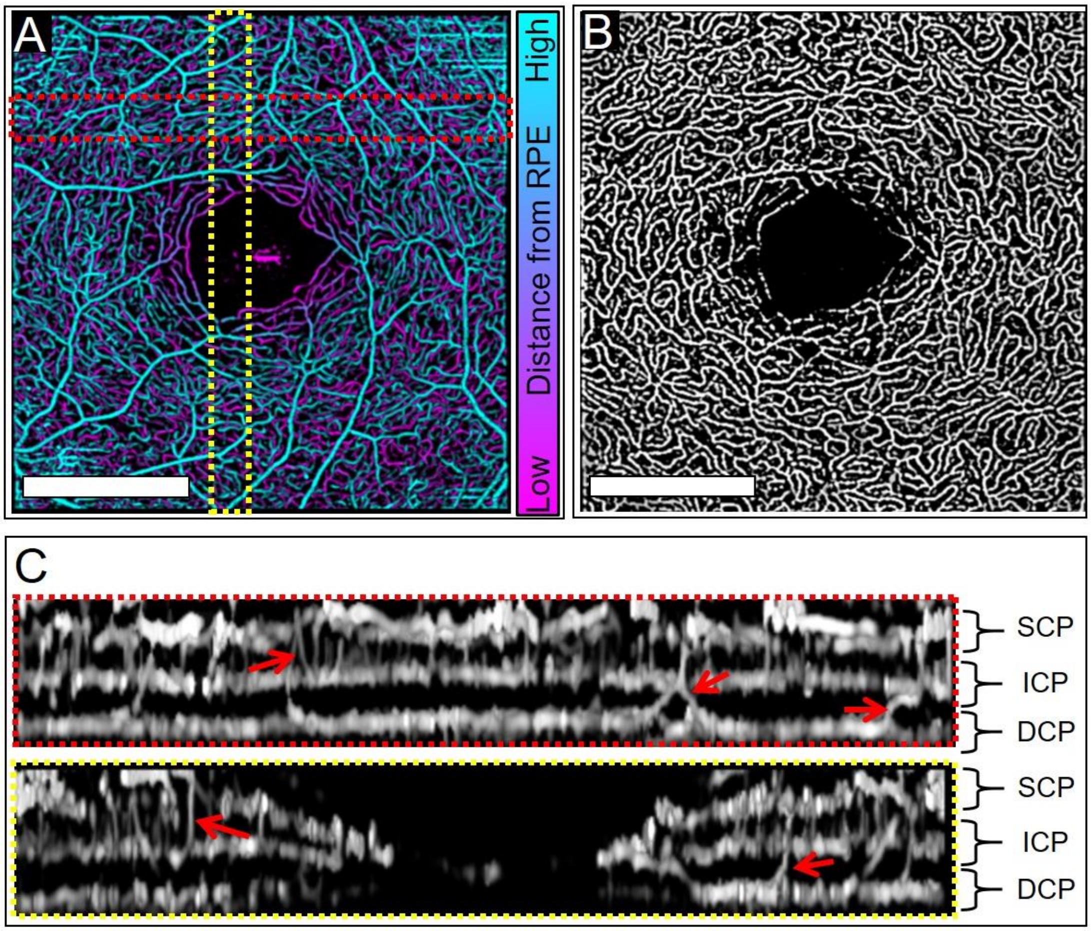

Figure 2.7. 3D vessel from Optimally Oriented Flux applied on unnormalized OCTA. Simple Otsu thresholding on the OOF response was used to generate a 3D vessel mask. (A) Depth color coded OOF response. Its DCP 3D vessel mask was shown in (B). Projection artifacts from superficial vessels are suppressed in the DCP 3D vessel mask. (C) Cross-sectional views of the 3D OOF response. Red arrows denote inter-plexus connections.

2.4.5 Graph representation and temporal autocorrelation decay measurements

Since the individual capillary segment is the largest spatial domain where uniform blood flow speed can be assumed, voxel location for every individual capillary segment need to be identified for the spatial compilation of the OCTA measurements.

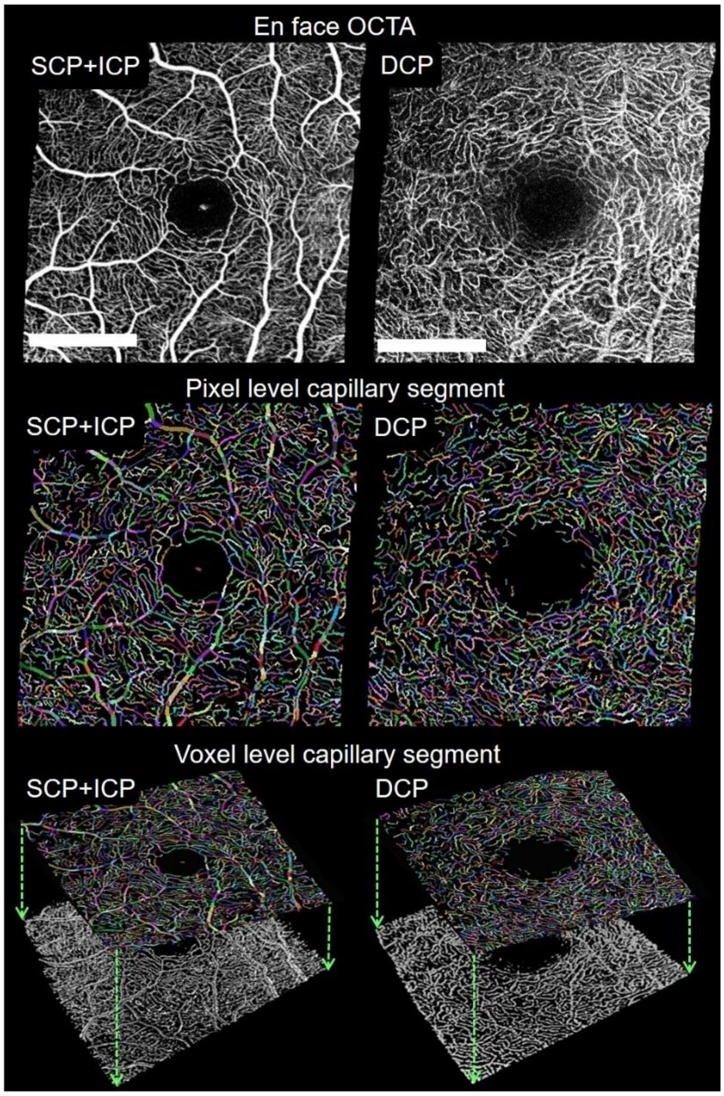

Figure 2.8. Voxel level capillary identification. Top: En face OCTA of superficial and intermediate capillary plexuses (SCP + ICP) and deep capillary plexus (DCP), generated from projection the unnormalized OCTA. Middle: Graph representation of the 2D en face OCTA. Vessel segments are denoted with different colors according to their identifiers (IDs). Bottom: Projecting the IDs from the 2D en face OCTA to the 3D vessel mask for voxel level capillary identification. Scale bars: 1 mm.

This voxel level capillary identification was achieved by assigning unique identifiers (ID) during pixel level capillary identification, and then projecting these capillary IDs on the 3D vessel mask produced from the OOF response. In pixel level identification, the Hessian based vesselness response proposed by Jerman et al. was applied on the en face OCTA [55]. This was applied separately for SCP + ICP, and DCP. The global Otsu threshold from the logarithm of the vesselness response was used to produce an en face vessel mask. This 2D vessel mask was skeletonized and turned into a graph, where the links represent center lines of the vessel and the nodes represent vessel bifurcation points [56]. All 2D vessel pixels of the en face OCTA were given a corresponding vessel ID, using MATLAB's 'bwdist' function. Different color notes different vessel ID in Fig. 2.8. The vessel ID of each pixel was projected on the corresponding 3D vessel mask. The same retinal layer segmentation was used to generate separate 3D vessel masks for SCP + ICP and DCP.

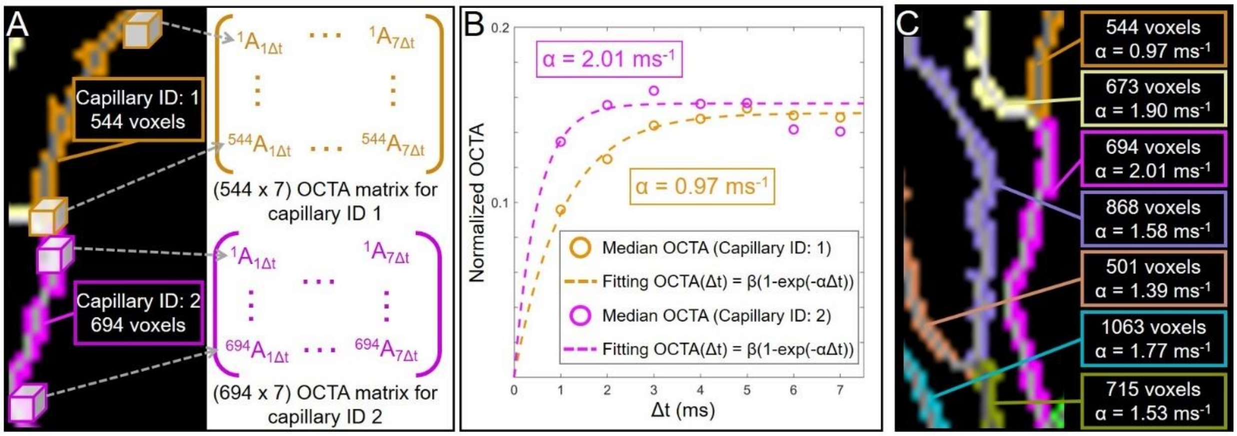

Figure 2.9. OCTA compilation and temporal autocorrelation decay constant evaluation. (A) OCTA measurements from each capillary are spatially compiled according to capillary ID. The compiled measurements can be represented as an OCTA matrix. (B) Fitting the representative OCTA at each interscan time to the OCTA saturation model. The temporal autocorrelation decay constants (α) are evaluated for individual capillaries. (C) The number of voxels and α of different capillaries.

After voxel level capillary identification, normalized OCTA measurements for each capillary segment was compiled for OCTA saturation characterization. Compiled normalized OCTA measurements of a capillary segment, comprised of M voxels with an OCTA protocol with N B-scan repeats, can be represented with an $M \times (N - 1)$ OCTA matrix. Medians of the normalized OCTA matrix columns, corresponding to $(N - 1)$ interscan time points, were fitted to $OCTA_{normalized}(\tau) = \beta\ (1 - \exp(-\alpha\tau))$ to evaluate the temporal autocorrelation decay constant, α, at individual capillary level (Fig. 2.9). The MATLAB fit function was used with 'Weights' option

[(N - 1), (N - 2), … 1], following the number of OCT pairs used for OCTA computation at each interscan time accounting for non-uniform SNR.

2.4.6 Choriocapillaris

Choroidal vasculature includes lobular structures as well as thick vessels. Therefore, choroidal vasculature does not have a single distinct spatial domain, such as capillary segments of the retinal vasculature, where we can assume uniform blood flow speed. Therefore, OCTA measurements for evaluating α should be spatially compiled with a different spatial domain. Here, a rectangular cuboid (53 μm × 53 μm in transverse plane and 8 μm in axial direction) was adopted as the spatial domain for the compilation. The transverse size of the cuboid is smaller than size of lobules observed in choriocapillaris. As in the retinal vasculature, the normalized OCTA measurements were compiled for each cuboid and fitted to $\mathrm{OCTA}_{\mathrm{normalized}}(\tau) = \beta\ (1 - \exp(-\alpha\tau))$ for temporal autocorrelation decay constant evaluation.

2.4.7 Visualization of blood flow speed

In order to visualize the blood flow speed surrogate marker α with en face OCTA, an HSV colormap (Hue, Saturation, Value) was used, following our previous implementation of variable interscan time analysis (VISTA) [37]. In Figure 2.9, the median filtered (window size: 5 × 5 pixels) α between [0.1 ms^{-1}, 2.5 ms^{-1}] was linearly mapped to hue between [0.67, 0], which corresponds to [blue, red]. En face OCTA from unnormalized OCTA was used for value in HSV and saturation was fixed to 1. Since unnormalized OCTA has a high dynamic range, the square root of en face OCTA was used for inner retinal vasculature for visualization purpose. Note that the hue was determined by the saturation characteristics of normalized OCTA, while the value (intensity) was determined by unnormalized OCTA (Fig. 2.10).

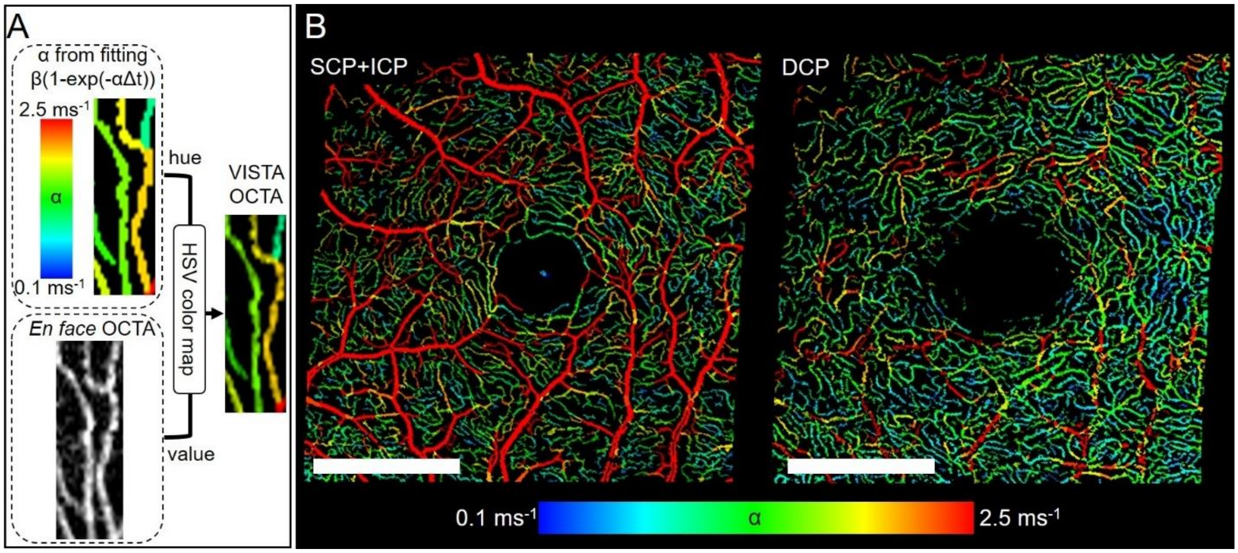

Figure 2.10. Visualization scheme. (A) HSV color map was adopted to generate pseudo-colored en face OCTA. The evaluated temporal autocorrelation decay constant was mapped to hue to provide blood flow speed information. (B) VISTA OCTA of SCP + ICP and DCP. Scale bars: 1 mm.

2.4.8 Limitations in visualization

When images are meant for human readers, choosing a color scheme that is perceptually uniform is crucial, especially in clinical applications [57, 58]. Unfortunately, the current linear mapping in between α and hue used in VISTA is not perceptually uniform [59]. This needs to be addressed as flow impairment and alterations in retinal capillaries can be subtle especially in the early stage of pathologies, and perceptually non-uniform colormaps can introduce colormap-derived perception of changes. If the blood flow speed surrogate marker is of only interest, the marker can be mapped to a perceptually uniform colormap after converting enface OCTA into a binary mask. However, this could be not ideal if the brightness variation in enface OCTA carries important information. A possible choice is a diverging colormap which can visualize scalar measurement perceptually uniform and also afford visualization of shading in 3D. Brightness variation in enface OCTA could be treated as shading, while the blood flow speed marker is mapped to the diverging colormap. For example, ‘Smooth cool warm’ would keep the correspondence between [red, blue] and [fast, slow], while mapping in the middle to bright gray. However, note that bivariate perceptually uniform continuous colormaps are not available.

Chapter 3

Pulsatility in the retinal vasculature and its compensation

3.1 Pulsatility in the retinal vasculature from adaptive optics

Retina blood flow measurements over a several second acquisition time are subject to pulsatile flow variation due to the cardiac cycle. In OCTA acquisition, multiple B-scan repeats are acquired before the next B-scan. Therefore, the pulsatility is encoded mainly in the slow scan direction. While the pulsatility can be an important biomarker itself, it is desirable to develop techniques which compensate pulsatility in order to simplify studies involving blood flow speed quantification or visualization.

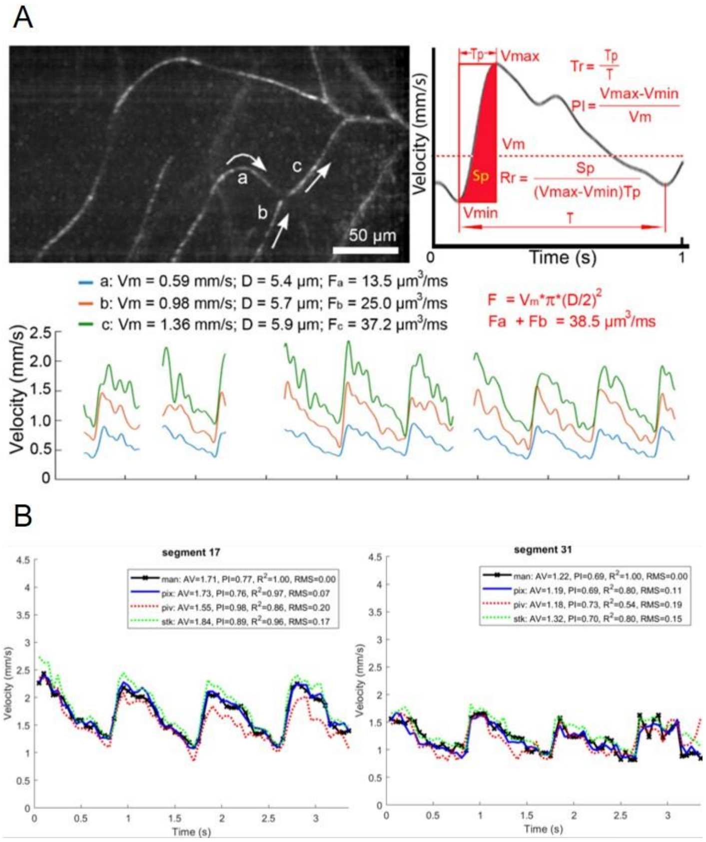

Figure 3.1. Pulsatility in human retinal capillaries from adaptive optics studies. (A): Human retinal capillaries imaged with an AO near-confocal ophthalmoscope. Three capillaries were chosen and their velocity over time is plotted in the bottom panel, which shows prominent

pulsatility. The image is from reference [45]. (B): Pulsatile modulation of blood flow speed in two different capillaries. The graph shows a rapid rise followed by a slower decrease of the speed. The image is from reference [46]. The ratio of maximum to minimum velocity during a pulsatile modulation reaches approximately 2.

Adaptive optics studies have shown that in human retinal capillaries, the ratio of maximum to minimum velocity in the cardiac cycle can be larger than 2 [45, 46] (Fig. 3.1). Therefore, pulsatile variations in blood flow speed can complicate studies if flow speed abnormalities caused by pathology are comparable or smaller to the pulsatile effects. While the capillaries show a considerable synchronization in their pulsatility, they still demonstrate both magnitude and temporal heterogeneity.

3.2 Pulsatility modeling

Pulsatility of the temporal autocorrelation decay constant α at the capillary segment level can be modeled by introducing a time varying scale factor.

$$\alpha^{(i)}(t) = \alpha_0^{(i)} \left(1 + g(t) \right) \text{ with } \overline{g(t)} = 0 \qquad \text{Eq. 3-1}$$

$\alpha^{(i)}_0$ is the time-averaged temporal autocorrelation decay constant of a capillary segment (i) and the cardiac cycle pulsatility is modeled with a pulsatility scale factor $g^{(i)}(t)$ whose time average is zero. A pulsatility compensation scheme aims to evaluate the $g^{(i)}(t)$ at the time of imaging to retrieve the $\alpha_0^{(i)}$,

$$\hat{\alpha}_0^{(i)} = \alpha^{(i)}/(1+\hat{g}) \qquad \text{Eq. 3-2}$$

$\alpha^{(i)}$ is the temporal autocorrelation decay constant evaluated without pulsatility compensation and $\hat{g}$ is the estimated pulsatility scale factor at the time the capillary was imaged.

3.3 Pulsatility in VISTA measurements

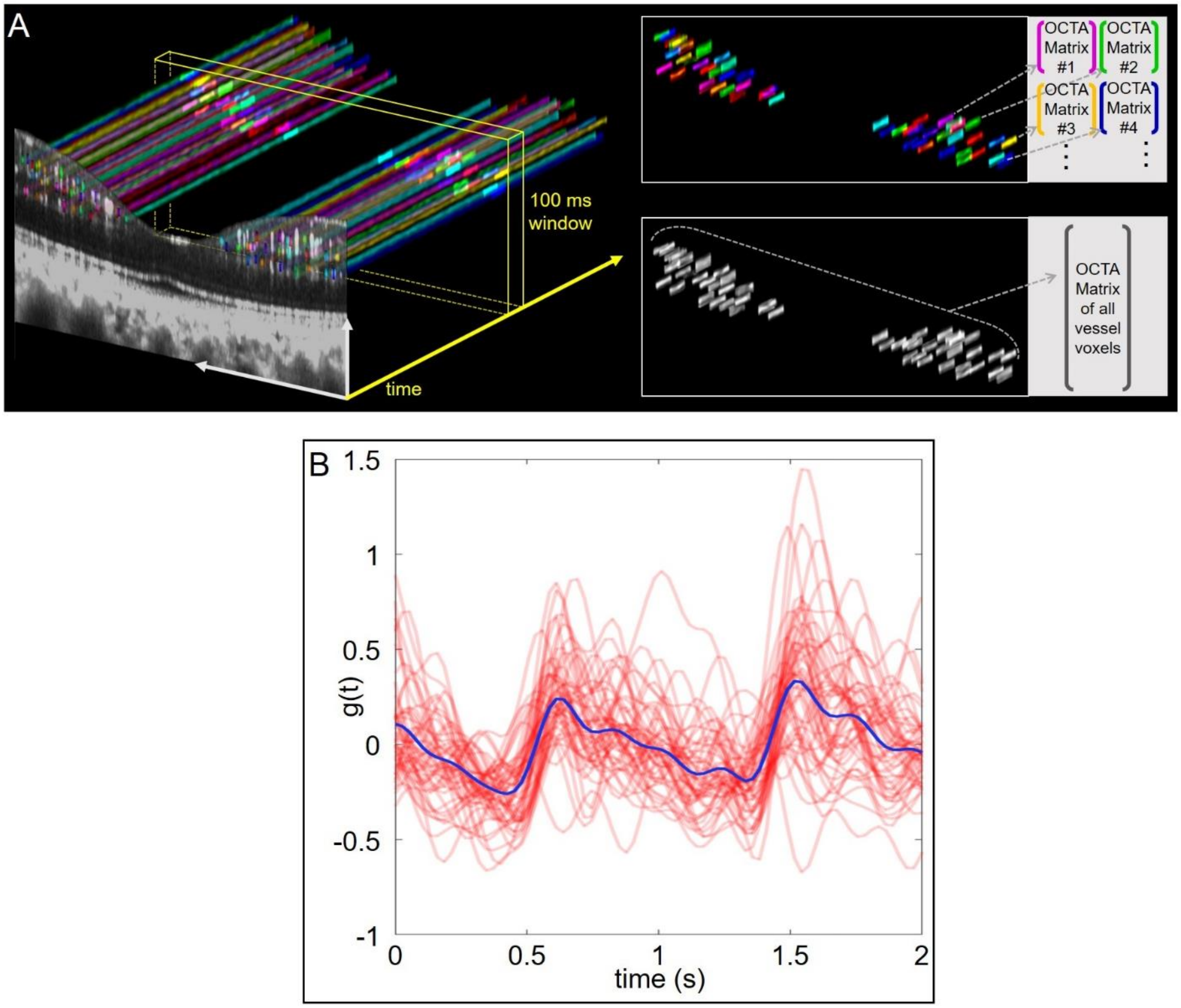

Figure 3.2. Pulsatility of temporal autocorrelation decay constants at individual capillaries. (A) The B-scan repeats at the fovea for 2 seconds. Individual capillary cross-sections are color-coded. The 100 ms time window enables spatial-temporal compilation of the capillaries and evaluation of temporal autocorrelation decay constants over time. (B) Pulsatility factors g(t) of the capillaries are plotted red. While synchronized, there is a significant heterogeneity in both phase and magnitude. The representative pulsatility factor is plotted blue.

To characterize the pulsatility of α measured with $\text{OCTA}_{\text{normalized}}(\tau) = \beta\ (1 - \exp(-\alpha\tau))$ fitting, the same B-scan location through the fovea of a healthy subject was repeatedly imaged. The total acquisition time was 2 seconds with 1 ms interscan time (2000 B-scans of 3 mm length with 450 A-scans/B-scan). The acquired data is essentially an OCT volume which encodes time along one axis. Eye movement was corrected using rigid translations between unnormalized OCTA, adopting the same scheme of isotropic FOV data. After eye movement correction, cross sections of vessels appear as straight tubular structures aligned to the time axis. OOF was applied to generate a 3D vessel mask, and ~50 capillary cross sections were selected from the cross section manually. Each cross section was tracked along the time axis in the OOF derived vessel mask, shown as different color tubes in Fig. 3.2A.

With a 100 ms time window, OCTA at interscan times from 1 ms to 7 ms were compiled and fitted to $\mathrm{OCTA}_{\mathrm{normalized}}(\tau) = \beta\ (1 - \exp(-\alpha\tau))$; the weight for fitting was equal for each time point since the number of OCT pairs used for different interscan time points are uniform. By sliding the 100 ms time window along the time axis, the time evolution of $\alpha(t)$ of each capillary and corresponding $g(t)$ were evaluated, where α_0 was set as the average value which zeroed the time-average of $g(t)$. Figure 3.2B shows the time evolutions of the pulsatility scale factors $g(t)$ of the segmented capillaries over 2 seconds, showing clear cardiac pulsatility at individual capillary level. The pulsatility scale factors for the capillaries show a certain degree of synchronization but demonstrate both phase (temporal) and magnitude heterogeneity. In general, the pulsatility factors have fast rise followed by slow recovery. The general shape and the existence of phase/magnitude heterogeneity are consistent with the pulsatile modulation of blood flow speeds in retinal capillaries reported in AO studies (Fig. 3.1).

While imaging the same location repeatedly allowed for the evaluation of individual capillaries pulsatility, OCTA protocols acquire a limited number of B-scans before imaging the next B-scan location. Since each capillary is imaged for a small portion of cardiac cycle, a representative pulsatility from the acquisition should be evaluated and approximated as pulsatility factors for each time point, encoded according to the B-scan indices.

3.4 Synchronization of pulsatility

Based on the synchronization of individual capillaries pulsatility, a method to extract a representative pulsatility, which can be later extended to pulsatility compensation in OCTA protocols with isotropic FOVs, is presented. OCTA measurements of all vessel voxels in the 100 ms time window, treating all the vessel voxels as one compiled vasculature, were spatially compiled (Fig. 3.2A). Then, the temporal autocorrelation constant from the 100 ms time window was evaluated, and its time evolution was evaluated by sliding the time window along the time axis. Since the compiled vasculature included all capillaries, the pulsatility of the compiled vasculature was labeled as the representative pulsatility, $g^{rep}(t)$.

The blue curve in Fig. 3.2B shows the pulsatility scale factor of the compiled vasculature, $g^{rep}(t)$, which demonstrates a fast rise followed by a slow recovery. The magnitude of $g^{rep}(t)$ is smaller than g(t) of individual capillaries, since compiling multiple capillaries which have different phases (i.e. temporal delays) blunts the rise and fall of $g^{rep}(t)$. However, the compilation still preserves the overall pulsatile variation.

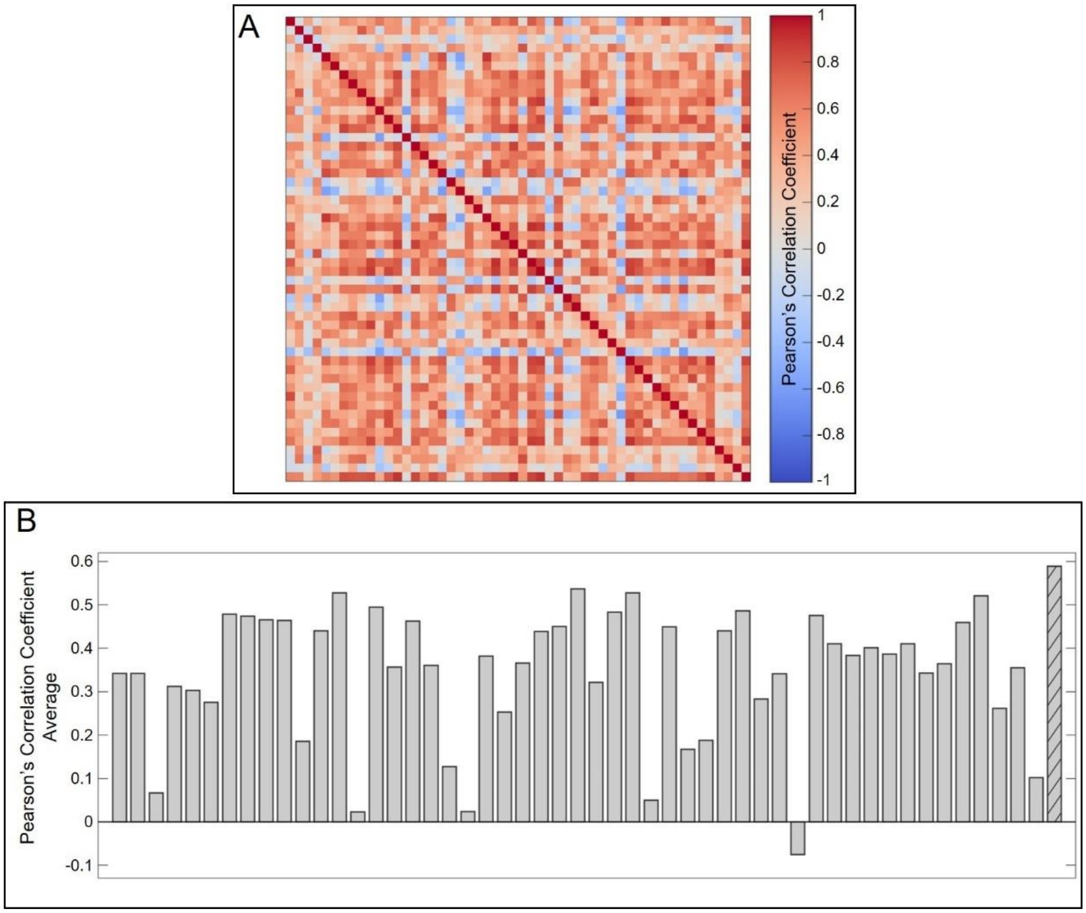

Figure 3.3. Quantifying synchronization of pulsatility between retinal capillaries. (A) Correlation matrix of g(t) of individual capillaries. The right-most column and bottom-most row represents $g^{rep}(t)$. (B) Bar graph showing average Pearson's correlation coefficients with other capillaries. The right-most bar (patterned) represents $g^{rep}(t)$.

Pearson's correlation coefficients among g(t) of individual capillaries and $g^{rep}(t)$ were evaluated to characterize: i) the degree of pulsatility synchronization and ii) how well $g^{rep}(t)$ represents pulsatility of individual capillaries. The average correlation coefficient of g(t) with other capillaries is shown in Fig. 3.3, which shows that a few individual capillaries showed little correlation with other capillaries. The average correlation of $g^{rep}(t)$ with other individual capillaries was 0.589.

3.5 Pulsatility compensation in an isotropic FOV

In the repeated B-scan acquisition over 2 second, the 100 ms time window was used to evaluate the representative pulsatility by compiling all vessel voxels in the time window. A general method that can extract the representative pulsatility for OCTA protocols with arbitrary FOVs and a pulsatility compensation scheme are presented.

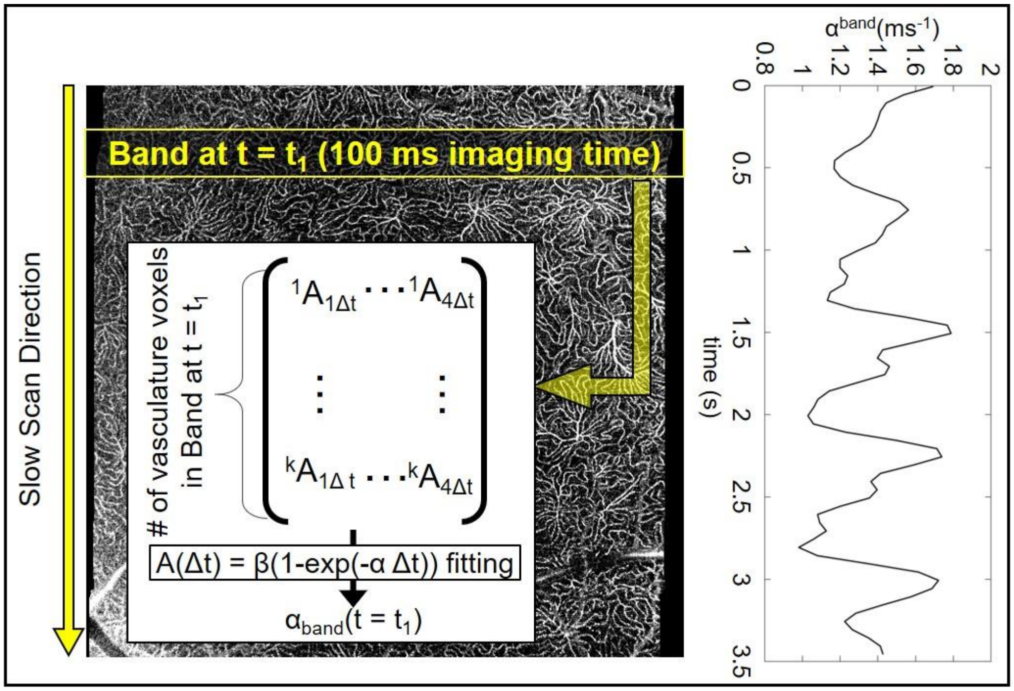

Figure 3.4. Evaluation of $g^{band}(y_n)$ as a representative pulsatility in an isotropic FOV OCTA. A band that includes all B-scans that are imaged within 100 ms is used. All vessel voxels in the band are identified, and their OCTA measurements are compiled. The identical OCTA saturation model was used to evaluate α^{band}. By sliding the band in the slow scan direction, the pulsatility encoded in time is extracted (the plot on the right is aligned with the en face OCTA on the left). Note that the α^{band} plot shows a clear pulsatility.

In OCTA protocols with isotropic FOVs, the slow scan axis encodes both i) time evolution and ii) spatial sweep of the retina in the slow scan direction. Assuming the pulsatility is uniform across the FOV, the slow scan direction encodes essentially only time evolution of the pulsatility. Therefore, temporal autocorrelation coefficient was evaluated from OCTA measurements compiled over a "band" that covers 100 ms imaging time, treating all vessel voxels in the band as one compiled vasculature. Sliding the band in the slow scan direction characterized the time evolution of the representative pulsatility. The pulsatility of $\alpha^{band}(y_n)$, where y_n is the slow scan index of the band, is the representative pulsatility where the slow scan index encodes the time linearly ($t_{imaging} = y_n N \Delta t$). The representative pulsatility $g^{band}(y_n)$ was then used for pulsatility compensation using the following equation.

$$\hat{\alpha}_0(x_n, y_n) = \alpha(x_n, y_n)/(1 + g^{band}(y_n)) \quad \text{Eq. 3-3}$$

x_n is the A-scan index in the B-scan, thereby assuming the pulsatility is constant over the B-scan repeats in the same location which is < 10 ms.

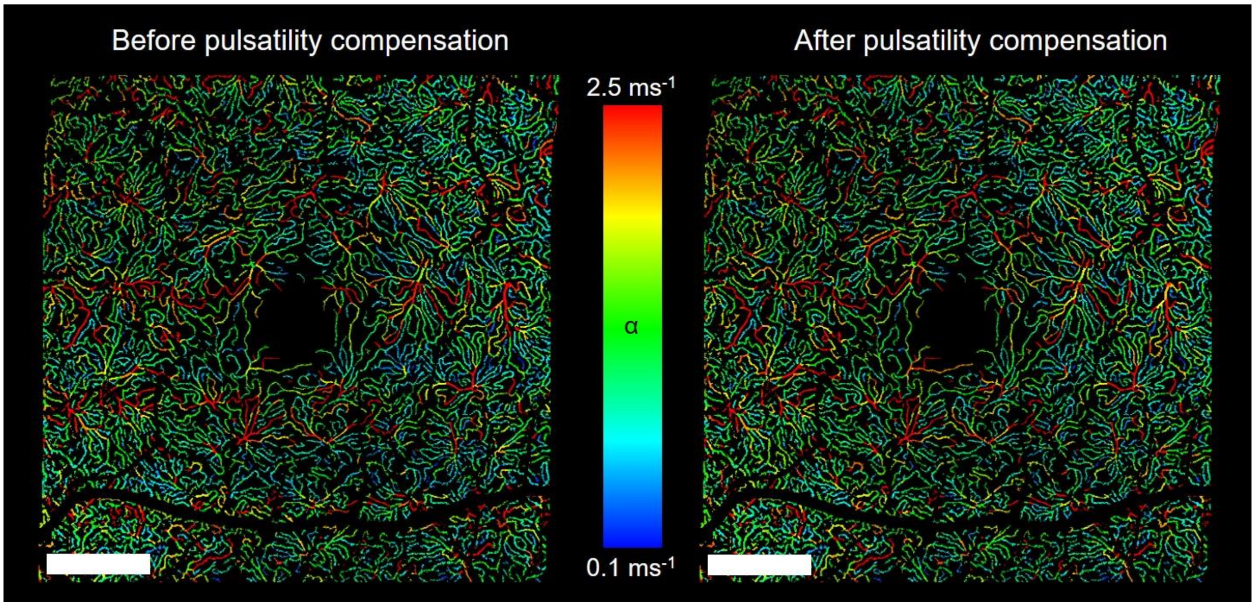

Figure 3.5. Pulsatility compensated VISTA. Left: Before the pulsatility compensation. Right: After the compensation. Scale bars: 1 mm.

Figure 3.5 shows an example of pulsatility compensation. Note that the presented method assumes that a pulsatility is uniform across the FOV and does not account for temporal and magnitude heterogeneity of the pulsatility among capillaries. On average, the representative pulsatility from the 100 ms imaging time band is expected to under-compensate the pulsatility, since compiling different vessel voxels is expected to reduce the magnitude of pulsatility from phase heterogeneity (Fig. 3.2). For choroidal vasculature, all voxels in the sliding band were treated as compiled vasculature and used to generate the representative pulsatility.

3.6 Limitations in pulsatility compensation

If there is eye motion or blinking, the pulsatility compensation may introduce artifacts which will limit OCTA compilation from the sliding band in the slow scan direction. Using the sliding band with a longer imaging time window may make evaluation of α^{band} more robust, at the cost of reduced time resolution. Also, our pulsatility compensation scheme assumes the same degree of pulsatility across FOV, which may not hold true if there are local lesions such as edema. Cardiac-gated multiple OCTA acquisitions can be used to reconstruct the pulsatile flow variations at all positions in the FOV [18]. However, this requires longer acquisition times and large datasets.

Chapter 4

Repeatability and compatibility

4.1 Repeatability

Four healthy subjects were imaged with the 3 x 3 mm protocol for 4 times. The subjects were instructed to sit back from the chinrest and the OCT prototype was realigned and the focus was adjusted each time. In order to evaluate repeatability at the capillary segment level, >100 individual capillary segments from SCP + ICP and DCP, respectively, were manually traced, and the corresponding capillary segments were identified in 4 repeated volumes from a healthy subject (Fig. 4.1). For each segment, α along the corresponding vascular skeleton was averaged to represent the α^{segment}. Figure 4.2 shows scatter plots of these four measurements.

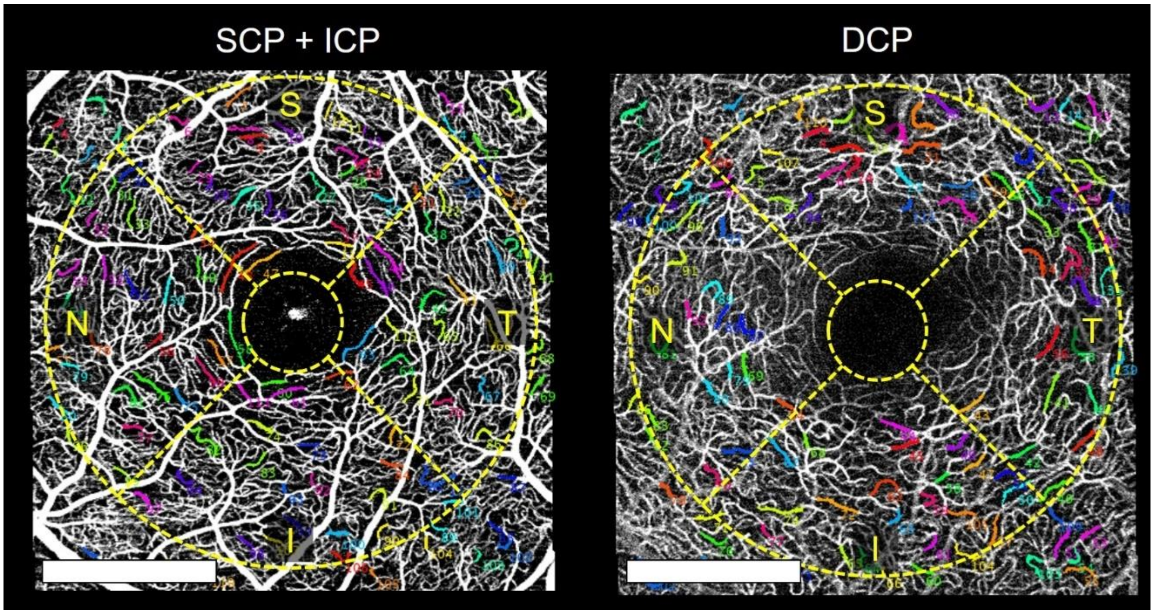

Figure 4.1. Segmented capillaries for repeatability evaluation. Color-coded segments represent manually traced retinal capillaries used for the capillary-level repeatability evaluation. Yellow dashed lines represent tracings for regional repeatability evaluation. S: Superior. N: Nasal. I: Inferior. T: Temporal.

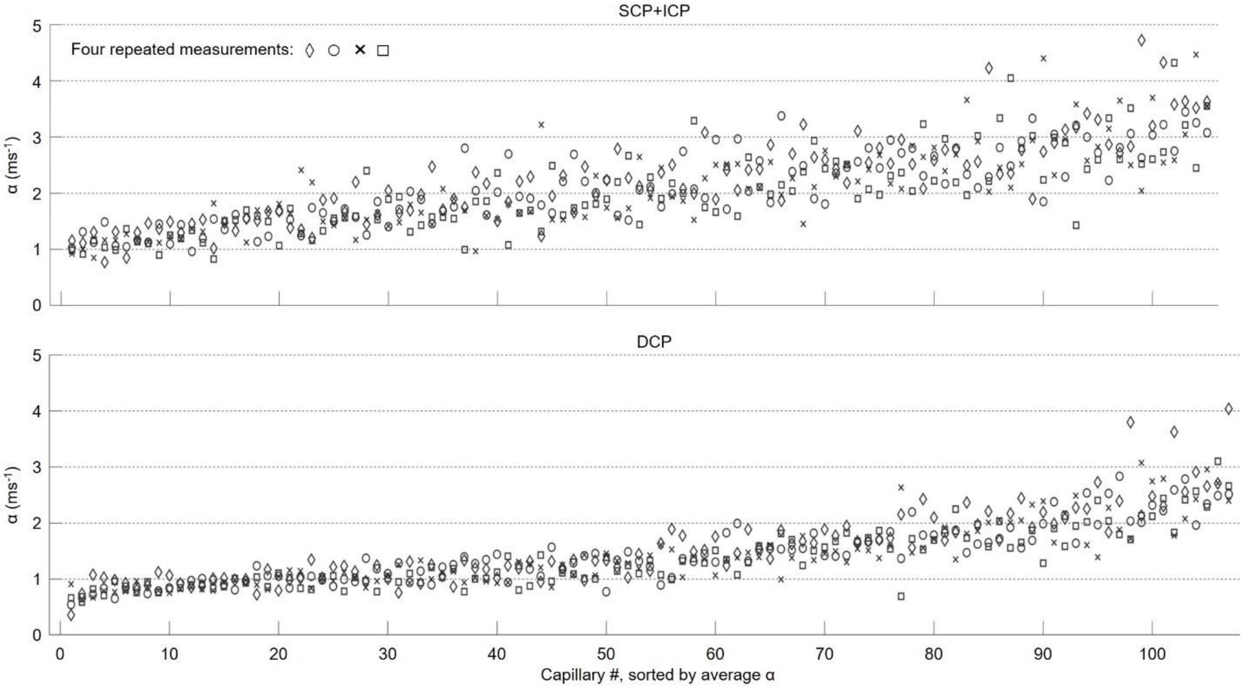

Figure 4.2. Repeated measurements at the capillary level. Different markers note different acquisitions. Top: superficial and intermediate capillary plexuses (SCP + ICP). Bottom: deep capillary plexus (DCP). The measurements are sorted by their average α from the four measurements. Note a significant range of α observed in different capillaries.

Figure 4.3 shows violin plots of the coefficient of variance (CV) from the repeatability evaluation. The [mean, median] of CV for individual capillary segment measurements were [0.194, 0.164] for SCP + ICP and [0.160, 0.154] for DCP. These are comparable to the reported CV of blood flow speeds in retinal capillaries measured using adaptive optics [60]. Nonetheless, note that VISTA measures the temporal autocorrelation decay constant in the vasculature, not the blood flow speed directly and the pulsatility compensation is likely to under-compensate the pulsatility since grouping different vessels together makes the pulsatility less sharp.

In order to evaluate repeatability at the regional level, four sub-regions (nasal, superior, temporal, inferior) from SCP + ICP and DCP were traced and subsequently identified in 4 repeated volumes each from 4 healthy subjects (Fig. 4.1). For each region, α at vascular skeletons in the region was averaged to represent $\alpha^{\text{sub-region}}$. The sum of 4 sub-regions was used to evaluate α^{global}. The CV of $\alpha^{\text{sub-region}}$ and α^{global} was below 0.075 and 0.05 respectively for both SCP + ICP and DCP and for all subjects (Fig. 4.3). To examine the dependence of repeatability on pulsatility compensation, the CV of α^{global} without pulsatility compensation was also evaluated. The CV was comparable to the case with pulsatility compensation; this is expected, since the overall effect of pulsatility compensation across the whole FOV will converge to unity and normal healthy subjects do not have local vascular lesions.

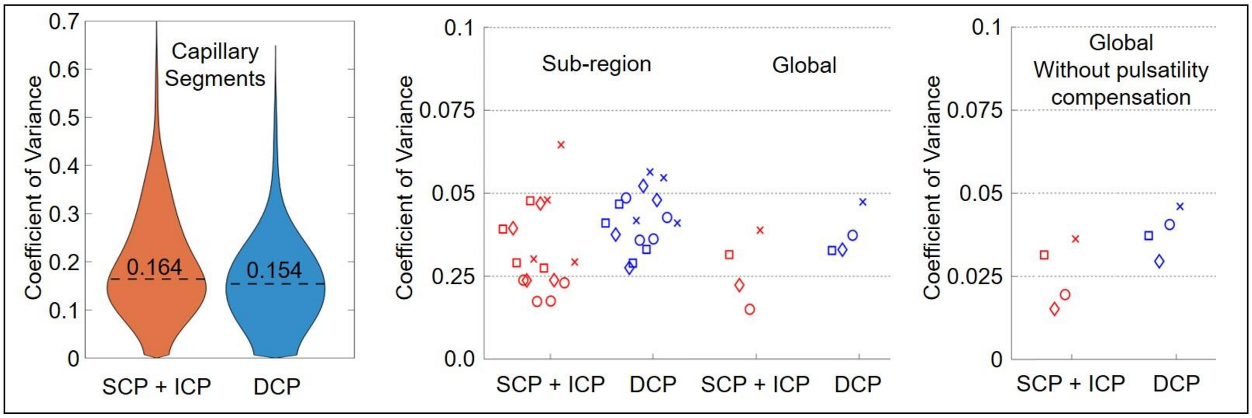

Figure 4.3. Repeatability of α measurements at multiple spatial levels. Left: Coefficient of variance (CV) of capillary segments. Middle: CV of sub-regions (Nasal, Superior, Inferior, Temporal) and global (N + S + I + T). Different markers are used for different subjects. The sub-region measurements are placed from the left in the order of N, S, I and T. Right: CV of global without pulsatility compensation.

4.2 Compatibility

Depending on the swept-source OCT A-scan rate, the target field-of-view (FOV), and galvanometer scan speed, the parameters for VISTA OCTA protocols can vary. Since temporal autocorrelation decay fitting and OOF vesselness response are the backbone of the new VISTA algorithm, key parameters for the algorithm include i) the fundamental interscan time, ii) the number of B-scan repeats and iii) the A-scan spacing. In order for the temporal autocorrelation decay constant α measured from VISTA to be a quantitative surrogate marker for blood flow speeds, α measured from different imaging protocols should be consistent, making different VISTA OCTA scan protocols compatible. One subject was imaged with both the 3 × 3 mm and 5 × 5 mm protocol (Table 2.1). The same capillary segments and regions marked for the repeatability evaluation in the 3 × 3 mm volume were identified in the 5 × 5 mm volume (Fig. 4.4).

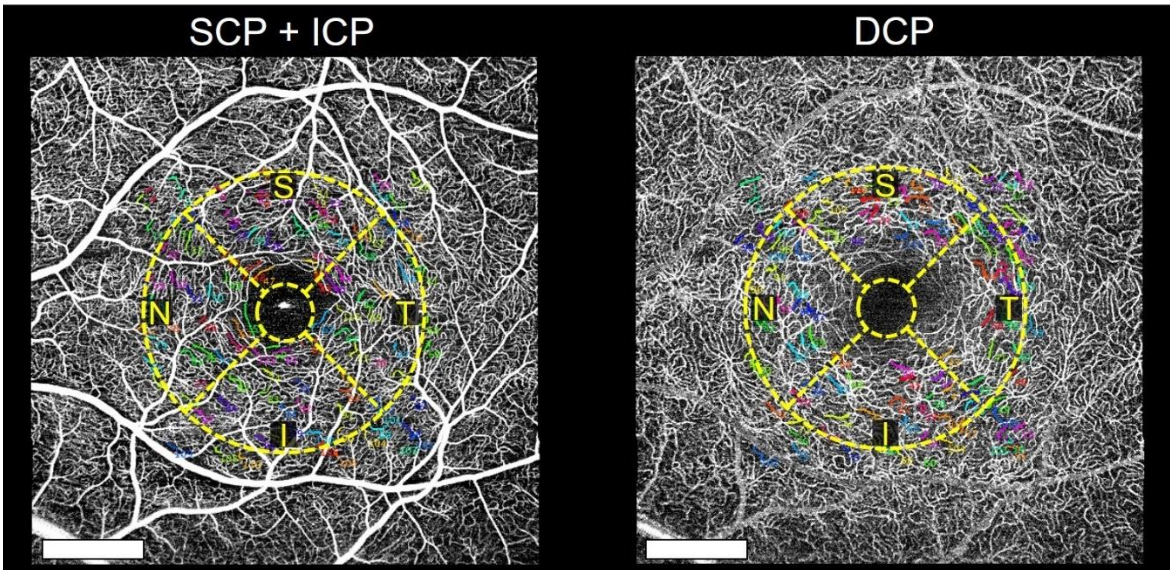

Figure 4.4 Capillaries and sub-regions identified in a 5 mm x 5 mm FOV en face OCTA to evaluate the compatibility of VISTA α measurements from different OCTA protocols. Scale bars: 1 mm

Figure 4.5 plots the $\alpha^{segment}$, $\alpha^{sub\text{-}region}$ and α^{global} measurements from the 3 × 3 mm protocol on x-axis and the 5 × 5 mm protocol on y-axis. Note that $\alpha^{sub\text{-}region}$ and α^{global} agree well. To examine the bias, such as consistent over or under estimation of α caused by different key parameters, 'y = kx' was fitted in between the two measurements. Fitting $\alpha^{segment}$ and α^{region} from the two protocols resulted in 'y = 0.969x' (dashed line in Fig. 4.5) and 'y = 0.979x' (solid line) respectively, indicating a small bias between the temporal autocorrelation decay constant measurements from the two scan protocols.

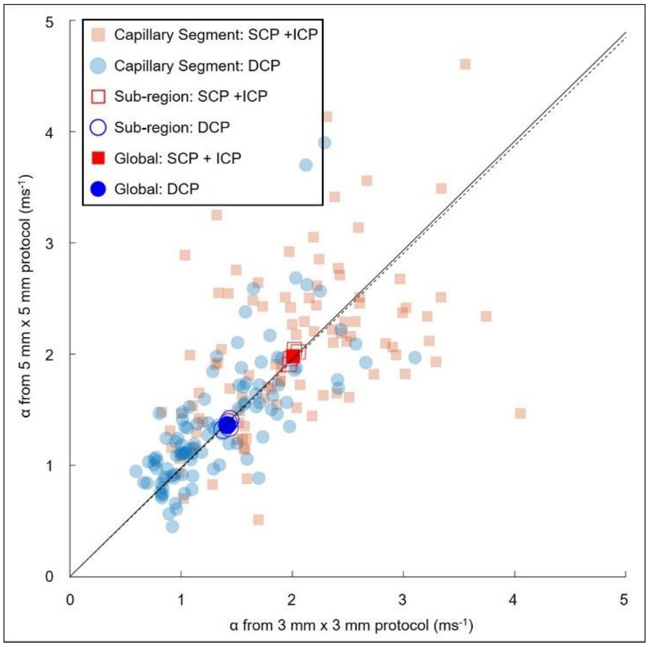

Figure 4.5. Scatter plots of VISTA α measurements from different OCTA protocols.

Chapter 5

Healthy retinal vasculature VISTA

5.1 Superficial + intermediate and deep capillary plexus

Hemodynamics characterization of different plexuses comprising the retinal vasculature may help understand how the vasculature supports the retina. The deep capillary plexus (DCP) shows distinct vasculature patterns from superficial and intermediate capillary plexuses (SCP + ICP), and it has been suggested that both SCP and ICP are directly supplied from arteries, while the DCP is supplied only through ICP [2]. To this end, as a quantitative surrogate marker for blood flow speed, the temporal autocorrelation coefficient α measurements in different plexuses were compared in healthy subjects.

For the temporal autocorrelation decay constant of a capillary plexus, α measurements from all capillaries are considered, by averaging α at vascular skeletons within the 1.5 mm eccentricity at each vascular plexus. The SCP + ICP showed faster autocorrelation decay constant than the DCP within the eccentricity of 1.5 mm for all repeated measurements. The ratios were near 0.7, and similar across the subjects (Fig. 5.1).

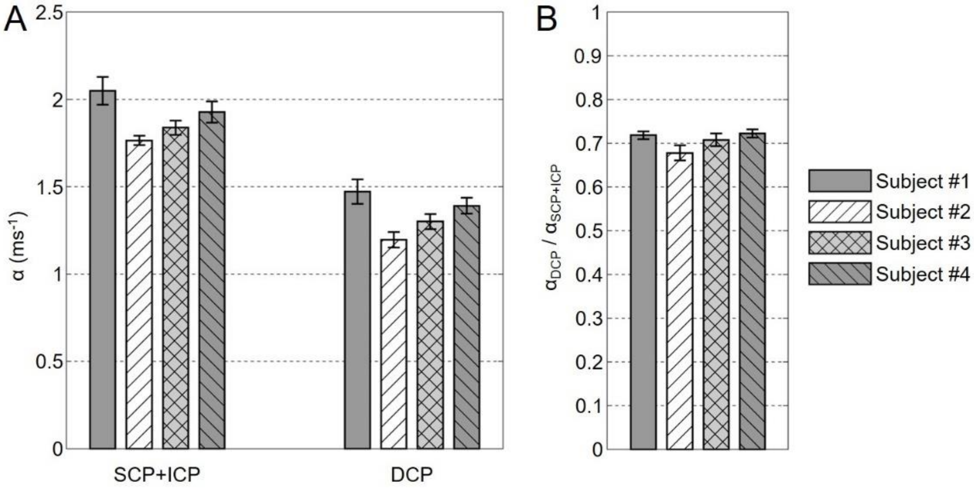

Figure 5.1. $\alpha^{\mathrm{SCP+ICP}}$, α^{DCP}, and their ratio in healthy subjects.

In a clinical setting, the transverse point spread function on the retina by OCT beam is unknown and dependent on cylindrical refractive error and aberration of the subject's eye, the axial eye length and the corneal drying. This can cause a variance in the temporal autocorrelation measurement using OCTA, since a large transverse point spread function is expected to experience a smaller degree of the temporal autocorrelation decay. $\alpha^{DCP}/\ \alpha^{SCP+ICP}$ is a self-normalizing biomarker that can offset the transverse point spread function variance. Intra eye, the point spread functions in the SCP and DCP are expected to be comparable, since the depth of focus is >400 μm and the distance between the plexuses is < 150 μm. Therefore, normalizing the α measurements from the DCP with the SCP + ICP may reduce the variance caused by the transverse point spread function variance across subjects.

5.2 Healthy retinal vasculature VISTA, between ONH and macula

Figure 5.2 and 5.3 show VISTA OCTA of 6 different vasculatures from one OCTA acquisition from a healthy subject, imaging the region between the optic nerve head (ONH) and the fovea. Segmentation of the RNFLP, SCP + ICP and DCP are shown with colors in Fig. 5.1. Consistent with the Fig. 5.1, the SCP + ICP has higher α than DCP. Notably, the RNFLP shows even lower α than the DCP. Distinct vortex-like and fern-like vascular patterns of DCP are marked with white arrowheads in Fig. 5.2B, which are likely to be the connections from the ICP. The centers of these vascular patterns often show high α in VISTA OCTA (arrowheads). To the author's best knowledge, this is the first visualization showing the differences of blood flow speed markers across the four capillary plexuses.

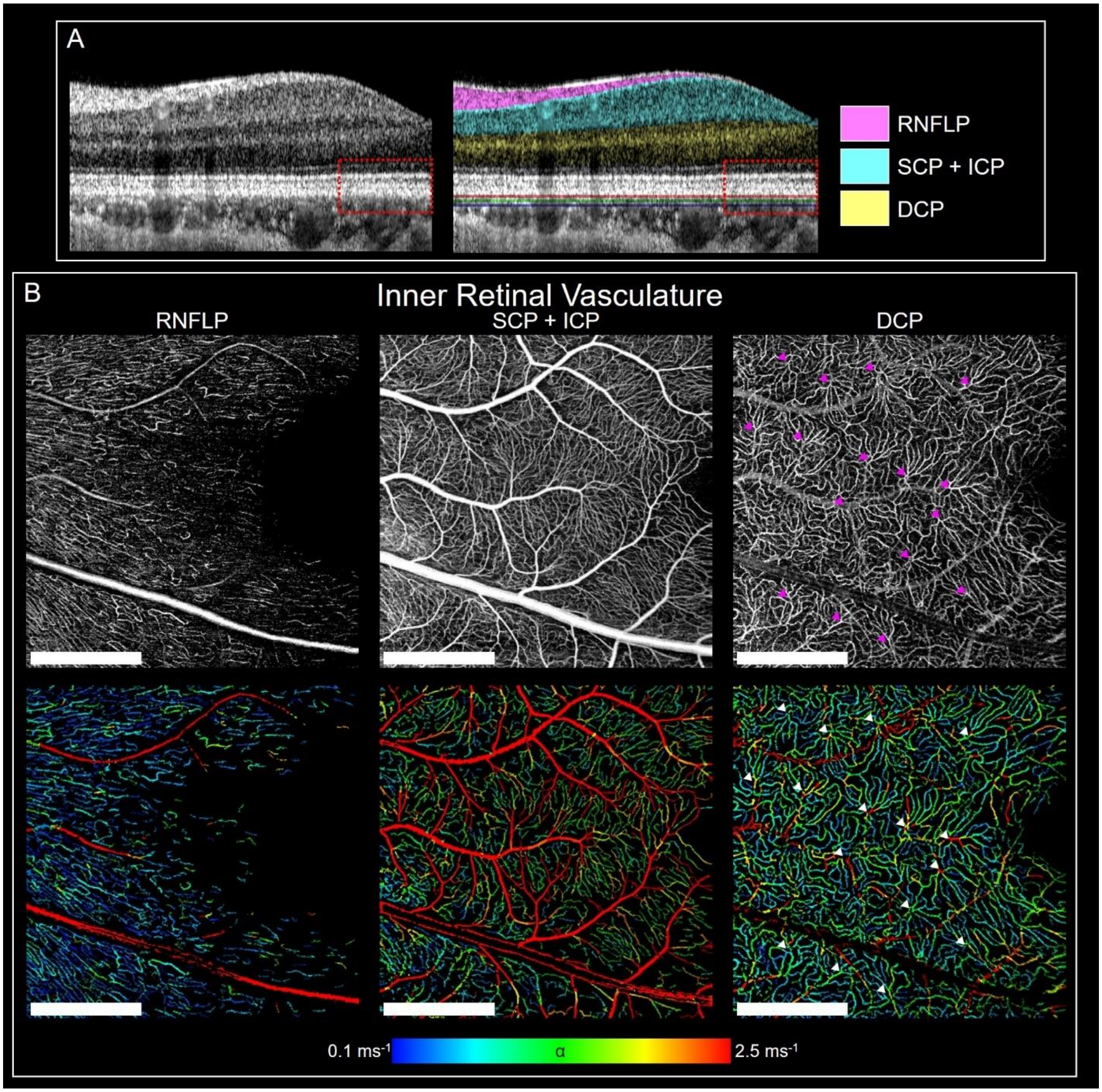

Figure 5.2. VISTA of different plexuses in between optic nerve head and fovea. (A) Segmentation of retinal vasculature into retinal nerve fiber layer plexus (RNLFP), superficial and intermediate capillary plexus (SCP + ICP), and deep capillary plexus (DCP). (B) Top: En face OCTA of each plexus group. Bottom: VISTA OCTA of each plexus group.

5.3 Healthy choroidal vasculature VISTA, between ONH and macula

Figure 5.3 shows the VISTA OCTA of the choroidal vasculature from the same volume. Segmentation of three choriocapillaris / choroidal slabs are visualized with color in Fig. 5.3A. Slabs 1, 2 and 3 are 13 μm, 27 μm and 40 μm posterior to RPE, respectively, with the slab 1 corresponding to the choriocapillaris. The thickness of the slabs is set 8 μm. Note that the axial resolution of the system is ~7 μm. En face OCTA from Slab 1 shows several lobular structures of the choriocapillaris. The centers of the lobules, which have maximal connection to the branches of each lobule, are marked with arrowheads in Fig. 5.3C. The large vessels posterior to the centers of lobules are observed in Choroidal Slab 2, marked with the same arrowheads. The diameters of these vessels are ~50 μm diameters. VISTA OCTA of Fig. 5.3 shows that the centers of the lobules in Slab 1 have higher α compared to the periphery of the lobules. This suggests that the center of lobular structures have higher blood flow speeds than the periphery of the lobules that is connected to the center. The large vessels below the lobules shown in Choroidal Slab 2 also show high blood flow speed. A larger vessel (~150 μm diameter) from Choroidal Slab 3 is marked with arrow heads, which has high α in VISTA OCTA (Fig. 5.3B).

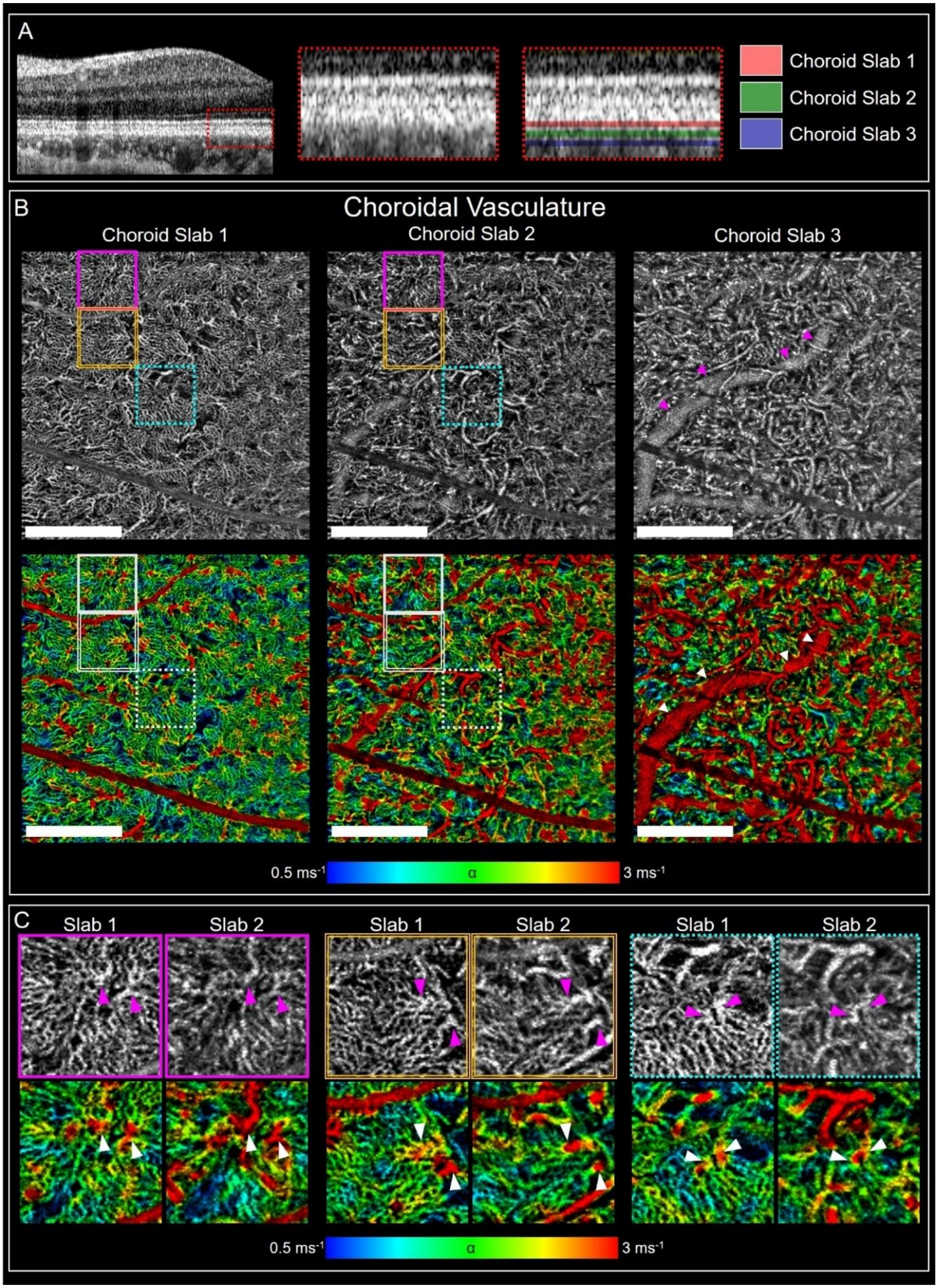

Figure 5.3. VISTA of choroidal vasculatures in between optic nerve head and fovea.

5.4 Healthy retinal and choroidal vasculature VISTA at macula

Figure 5.4 shows the VISTA OCTA of macula at a 5 mm x 5 mm FOV. Slower blood flow speed in the DCP compared to SCP + ICP is consistent. This shows that a 600 kHz A-scan rate can provide blood flow speed information of retinal vasculature covering the majority of the macula (5.5 mm in diameter) with one data acquisition.

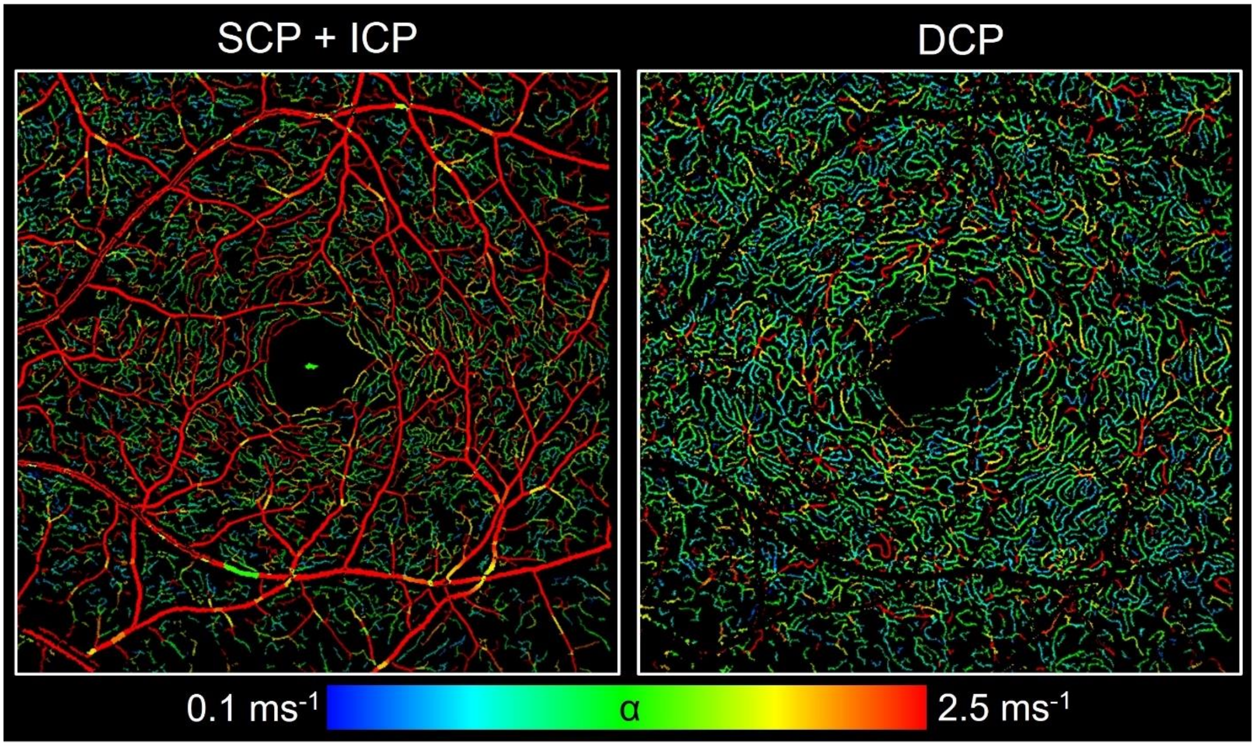

Figure 5.4. VISTA OCTA of macula with a 5 mm x 5 mm field-of-view.

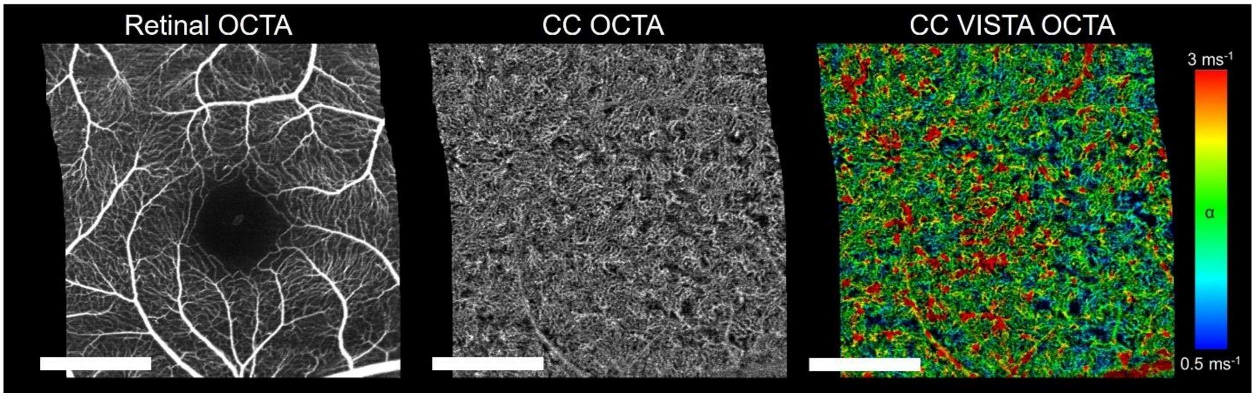

Figure 5.5. VISTA of choriocapillaris under the fovea. 3 mm x 3 mm field-of-view. Left: Retinal vasculature en face OCTA. Middle: Choriocapillaris en face OCTA. Right: Choriocapillaris VISTA OCTA.

Unlike between optic nerve head and macula as presented in Fig. 5.3, identifying individual lobules (or “honeycomb” structures) in the choriocapillaris under the fovea remains challenging. Figure 5.5 shows that with VISTA, there are high α regions that are scattered across the FOV in the choriocapillaris under the fovea. Since the center of the choriocapillaris lobules corresponded to the high α regions in between the optic nerve head and macula, the high α regions under the fovea may correspond to individual lobules or “honeycomb” structures that act as a functional unit of the choriocapillaris. Figure 5.6 shows that these scattered high α regions are observed across the whole macula.

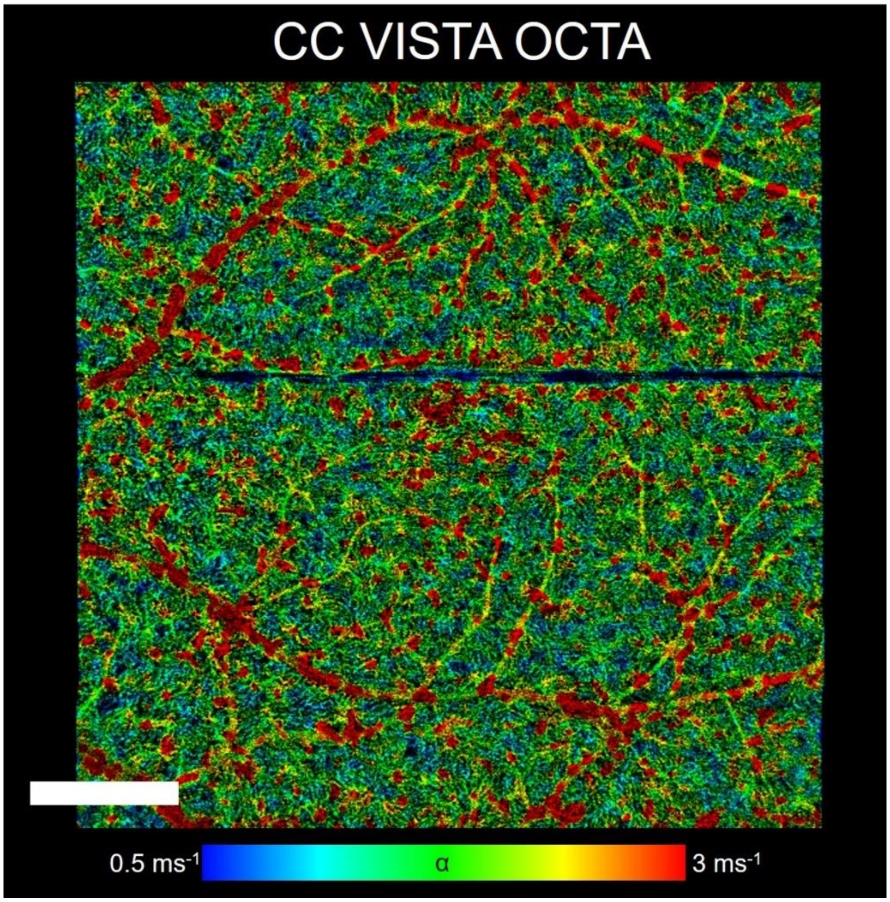

Figure 5.6. VISTA of choriocapillaris at macula. 5 mm x 5 mm. Scale bar: 1 mm.

Chapter 6

Diabetic retinopathy and AMD VISTA

6.1 Diabetic retinopathy and blood flow speeds

Diabetic retinopathy (DR) is the most common vascular complication of diabetic mellitus, and it is a leading cause of vision loss worldwide [61, 62]. Early features of the pathology include pericyte loss, thickening of basement membrane, and formation of microaneurysms. In DR, the vascular injury occurs primarily at the microcirculation level; the capillaries are the sites in the retina most frequently subjected to occlusion in DR. The damages to the vasculature may cause ischemia in the retina and the breakdown of the inner retinal blood barrier, leading to neovascularization and diabetic macular edema.

One of the microvascular injuries common in DR is capillary non-perfusion. Since OCTA readily visualizes capillaries, capillary non-perfusion manifests as a lack of vasculature in en face OCTA. The depth resolution of the imaging modality also enables investigation of capillary non-perfusion in different plexuses. The recent development of wide-field OCTA also showed that capillary non-perfusion is readily visualized outside the macula in DR as well [25, 63-65].

While the capillary non-perfusion can reflect the extent of ischemia that the retina is experiencing, the process itself is likely to be irreversible [66, 67]. Also, the binary characterization of the perfusion status does not provide information about the retinal blood barrier integrity of the perfused vasculature.

VISTA aims to complement the structure imaging of traditional OCTA by providing blood flow speed information. It is plausible that changes in the integrity of blood retinal barrier may also lead to changes in the fluid resistance of the vasculature. This may also manifest as changes in blood flow speed information. This indicates the potential of VISTA to characterize blood flow speed information associated with irreversible capillary non-perfusion, before the actual non-perfusion takes place.

6.2 Diabetic retinopathy VISTA

Figure 6.1 shows representative VISTA OCTA images of the SCP + ICP and DCP of eyes with mild, moderate and severe non-proliferative diabetic retinopathy (NPDR). Generally low α was observed in the mild NPDR eye.

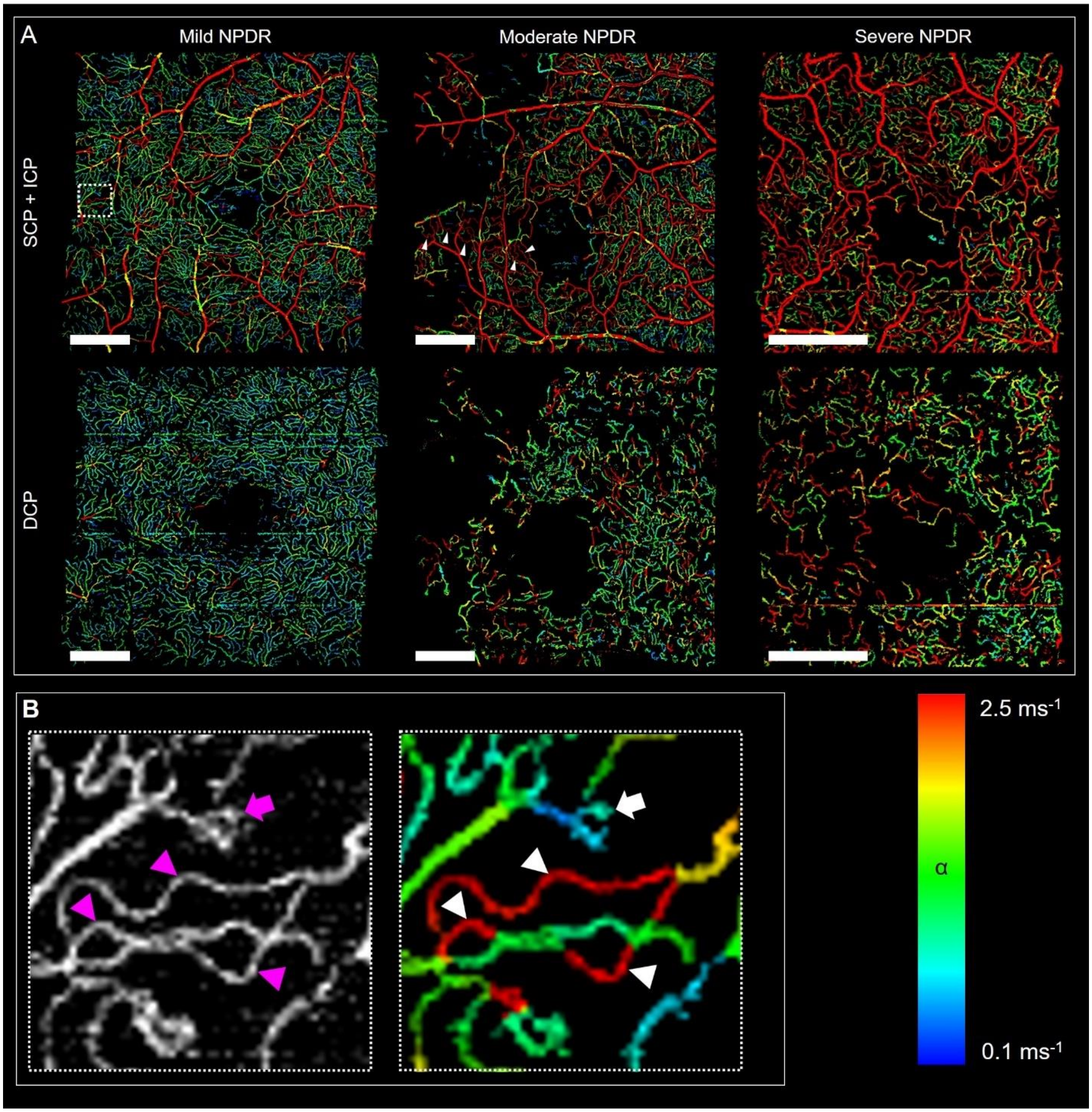

Figure 6.1. VISTA of non-proliferative diabetic retinopathy (NPDR). Scale bars: 1 mm.

Figure 6.1B shows an enlarged view of the SCP + ICP of the mild NPDR eye from a region with low capillary density. The tortuous vessels (arrowheads) and the focal bulge (arrow) have high and low α, respectively. In the moderate NPDR eye, the tortuous capillaries showed high α (arrowheads). The severe NPDR eye was anti-VEGF treatment naïve at the time of imaging, and high α, even in the DCP, was observed.

VISTA OCTA images of the SCP + ICP of proliferative diabetic retinopathy (treated) eyes are shown in Fig. 6.2. Note that even a few vessels significantly larger than capillaries in Fig. 6.2A have low α (arrowheads). Enlarged views of microvascular lesions such as capillary loops and microaneurysms show that VISTA OCTA provides blood flow speed information that is not available from standard OCTA. Note that en face OCTA and the ‘intensity’ (value of HSV colormap) of VISTA OCTA images are derived from unnormalized OCTA, and only the ‘color’ (hue of HSV colormap) is derived from normalized OCTA and its saturation characteristics.

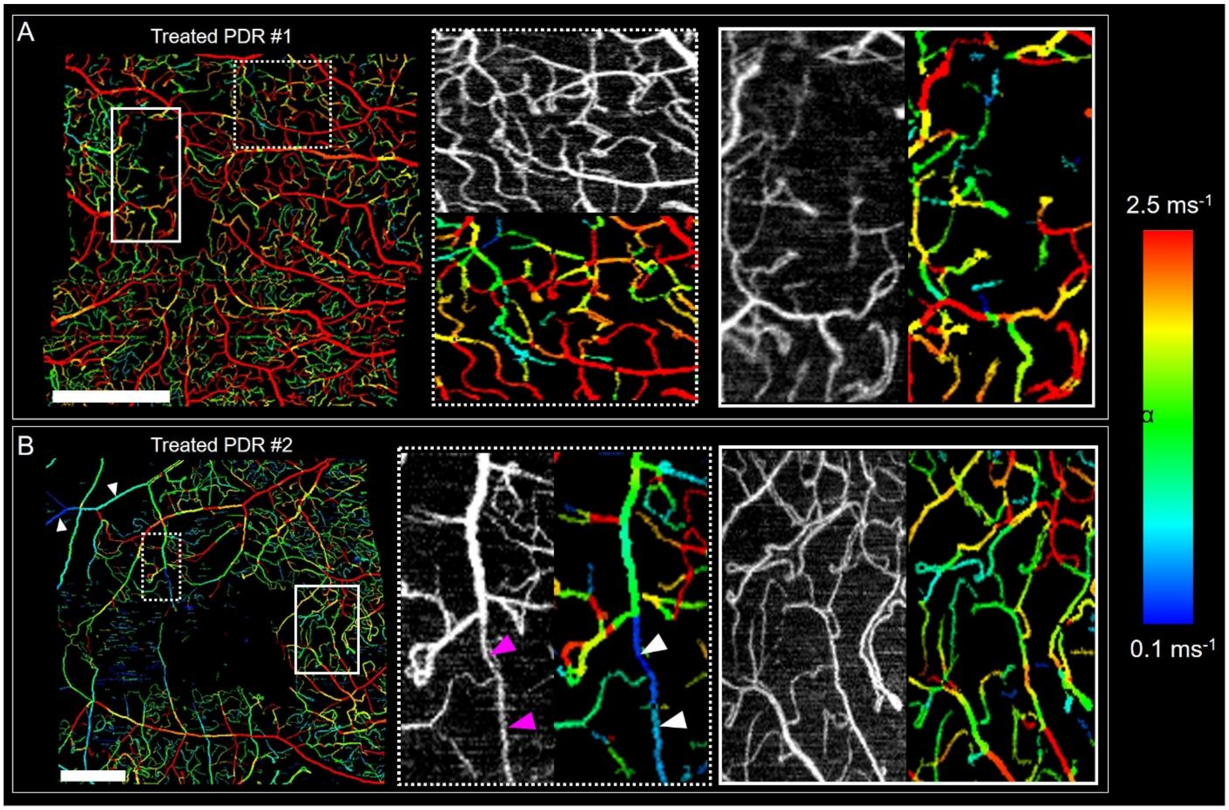

Figure 6.2. VISTA of proliferative diabetic retinopathy (PDR). Scale bars: 1 mm.

6.3 Age-related macular degeneration and blood flow speeds.

Age-related macular degeneration (AMD) is a leading cause of central vision impairment [68]. The pathology entails photoreceptors, retinal pigment epithelium and choriocapillaris. Drusen are extracellular deposits between the retinal pigment epithelium (RPE) and Bruch’s membrane. The number and size of drusen is used for determining stages of AMD [69, 70]. Drusen is also a prognostic marker in advancing to late stages of AMD. As a depth-resolved imaging modality, OCT has been crucial in the recent progress in understanding of drusen, including quantification and classification of drusen [71].

Choriocapillaris is responsible for oxygen and metabolite exchange for outer retina. The large distance between the outer retina and inner retinal vasculature likely makes choriocapillaris the only vasculature that supports the outer retina. While whether choriocapillaris or RPE is the driver of AMD is still a controversial topic, it is well accepted that choriocapillaris plays a role in AMD.

Therefore, with the development of OCTA, there has been significant effort in generating OCTA signals in choriocapillaris [72]. The source of contrast in choriocapillaris OCTA is identical as retinal vasculature OCTA: the displacement of red blood cells during the B-scan repeats.

While the principle is the same, choriocapillaris OCTA poses unique challenges that set it apart from retinal vasculature OCTA. First, choriocapillaris is under the RPE, which is highly scattering. This results in weak signal in choriocapillaris structure OCT signal, especially in the shorter wavelength. Since the OCTA signal is based on the fluctuation of OCT, the reduction in the OCT signal makes generating OCTA challenging. The 1050 nm beam is less impaired by this compared to 840 nm, and readily visualizes the structure under the RPE.

Another challenge is that the choriocapillaris is not hyper-scattering compared to the structures around it. In case of the retinal vasculature, the red blood cells and vessel walls are more hyperreflective compared to the surrounding tissue inner retina, which allows more light to reach the photoreceptors. Therefore, the structural signal alone can visualize inner retinal vasculature, and unnormalized OCTA generates high contrast image for the vasculature. However, anterior to the choriocapillaris is RPE, which is significantly more scattering than choriocapillaris; posterior to the choriocapillaris is Sattler’s layer, another component of choroidal vasculature with medium-sized vessels. Therefore, the choriocapillaris is not readily discernible in structural OCT or cross-section B-scans of unnormalized OCTA. Furthermore, the thickness of choriocapillaris is ~ 10 µm, not much larger than the axial resolution of 1050 nm OCT system (~ 7 µm). This makes the accurate segmentation of the choriocapillaris challenging. Current VISTA pipeline provides a 3D OCT volume that is inter B-scan registered based on unnormalized OCTA. This enables a robust segmentation of the RPE, and a consistent slab selection for choriocapillaris.

The last challenge is the morphology of choriocapillaris. The retinal vasculature is comprised of individual tubular segments. Therefore, the vesselness filter can be readily applied to enhance its visualization. Also, the retinal vasculature is sparse even when projected, facilitating generation of 2D vessel masks. In contrast, the choriocapillaris is fenestrated and densely packed.

Despite these challenges, OCTA has been used to study choriocapillaris in AMD. Choriocapillaris flow deficit (CC FD) is a widely studied biomarker based on the vasculature's OCTA [73, 74]. Studies have shown that CC FD is a prognostic marker of geographic atrophy progression, associated with macular neovascularization and development of drusen [31].

Blood flow speed quantification enabled by VISTA offers a unique angle to study choriocapillaris in AMD. By evaluating the temporal autocorrelation decay constant, Figure 5.3 shows the correspondence between the high blood flow speed and the center of the lobules. In the macula however, these lobular structures are less obvious. Still, the macula shows high α scattered across the FOV (Fig. 5.5). Since the high blood flow speed corresponded to the center of the lobules in the region between optic nerve head and macula, it is plausible that high alpha corresponds to a structure of the choriocapillaris that is responsible for blood flow supply or drain. In other words, the high blood flow speed region may mark the functional units of choriocapillaris. Unlike the fenestration of choriocapillaris which may need <10 μm transverse resolution to identify, the functional units of choriocapillaris – which are honeycomb or lobular structures – are size of >300 μm [3]. This indicates if the function of choriocapillaris – blood flow – can be visualized at ~50 μm spatial resolution, which is readily achievable for OCT and OCTA, individual functional units of choriocapillaris can be identified.

6.4 Age-related macular degeneration VISTA

Figure 5.6 shows that in the healthy macula, even though the en face OCTA does not provide readily identifiable units of choriocapillaris, VISTA OCTA visualizes high blood flow speed regions, manifested as red dots across the FOV. Figure 6.3 shows that in the case of AMD, such red dots are not scattered near the drusen, which show low α. This indicates that VISTA enables topographical study of the choriocapillaris blood flow speed. Note that since OCT readily provides drusen map, the spatial association between the drusen and choriocapillaris blood flow speed can be studied.

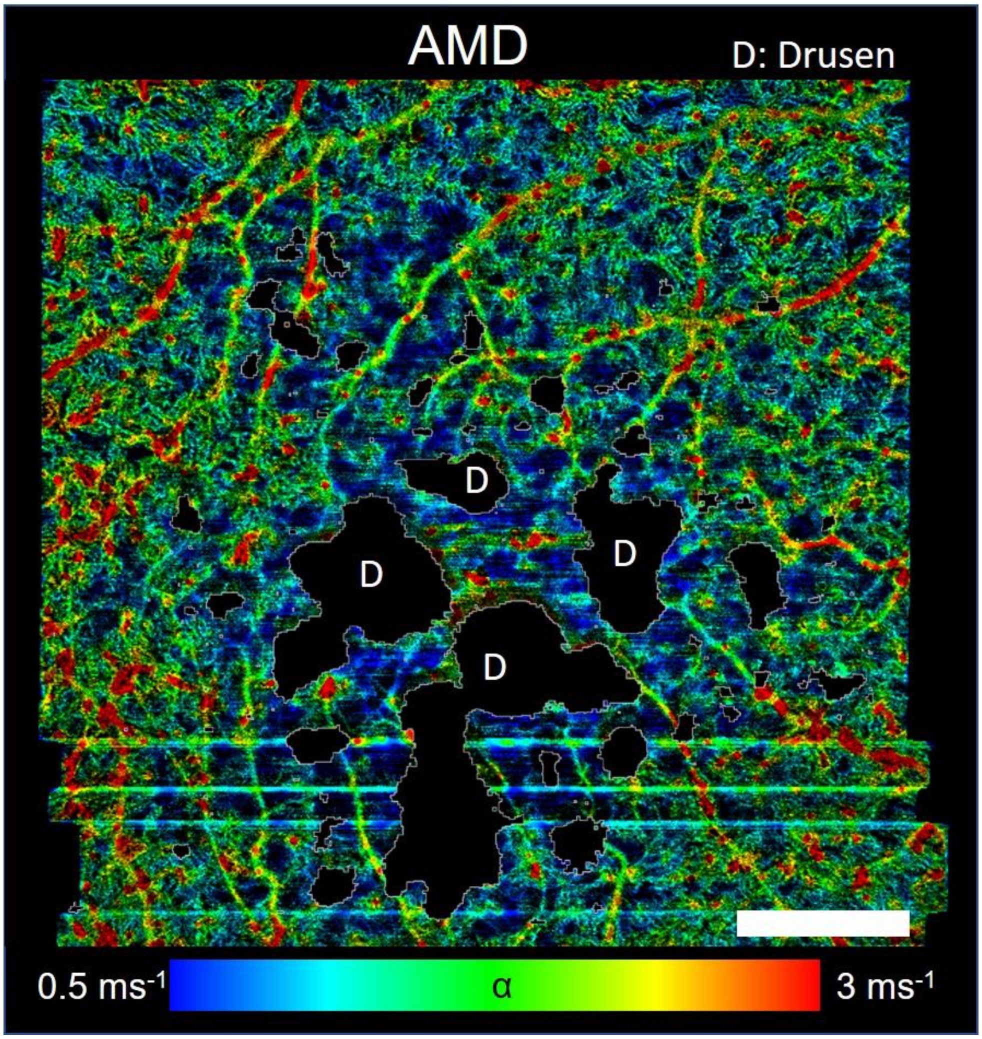

Figure 6.3 Choriocapillaris VISTA of age-related macular degeneration (AMD). D: Drusen map.

Chapter 7
Conclusion

7.1 Accomplished works

This thesis demonstrated the development of a second-generation variable interscan time analysis (VISTA) OCTA algorithm that provides a quantitative surrogate marker for blood flow speeds [75]. Swept-source OCT with a 600 kHz A-scan rate enabled clinically feasible imaging protocols with fine A-scan spacing, up to 5 mm x 5 mm field-of-views (FOVs), and OCTA at short interscan times (~1 ms), within a total acquisition time of 3.6 seconds. Normalized OCTA measurements at multiple interscan times were spatially compiled for each spatial domain, where uniform blood flow speed was assumed. Subsequently, the compiled measurements were fitted to an OCTA saturation model to evaluate a temporal autocorrelation decay constant α. Fine A-scan spacing enabled capillary identification at individual capillary segment level for spatial compilation of OCTA. VISTA OCTA measured α showed pulsatility in retinal capillaries that is consistent with the previous adaptive optics studies. A pulsatility compensation scheme applicable in isotropic FOV OCTA protocols was proposed. The repeatability of VISTA OCTA and consistency of α measurements from different imaging protocols were evaluated at multiple spatial levels. The regional measurements showed high repeatability and compatibility between different OCTA protocols.

VISTA can quantitatively characterize the blood flow speeds using a single global number, such as $\alpha^{SCP+ICP}$ or α^{DCP}, as well as with the distribution of α. The capability of VISTA to provide simple quantitative measurements for an eye, analogous to OCTA vessel density and foveal avascular zone area, simplifies interpretation and can facilitate longitudinal studies on progression or treatment responses. In addition, the new VISTA protocol still provides standard en face OCTA. This provides a natural connection between future VISTA studies and the existing extensive body of OCTA research.

Chapter 5 shows that VISTA enables studies of blood flow speeds in healthy normal retinal vasculature at the capillary level, while still providing multi mm^2 FOV, a scale significantly larger than a few selected vessel segments. To the best of the author's knowledge, comparing blood flow surrogate markers between the SCP + ICP and DCP has not been reported in humans in vivo. Clear visualization of the lobular structure of choriocapillaris with high α near the center of the lobules also suggests that VISTA can be applied to assess choriocapillaris flow status.

The shortest interscan time limit by the inertia of the galvanometer and keeping the total acquisition time under 4 seconds necessitated choosing a simple exponential decay model for the temporal autocorrelation decay. Assuming that $\rho(\tau) = \exp(-\alpha\tau)$ is a reasonable model for temporal autocorrelation decay in retinal capillaries, the α measurements of capillary plexuses provide guidance on the fundamental interscan time required for α evaluation using the VISTA algorithm. For example, consider a 3 ms fundamental interscan time using the same OCT beam size (1.4 mm 1/e2 diameter at pupil). At the shortest interscan time, the OCTA signal will already be >99% saturated in the SCP + ICP since the average α is ~2 ms^{-1}. Here, the author proposes using <95% OCTA saturation at the shortest interscan time, or $\exp(-\alpha\Delta t)>0.05$, as a phenomenological requirement evaluating the autocorrelation decay. This yields $\alpha_{max}\Delta t_{fundamental} \approx 3$; therefore, assuming the same beam size at the pupil as the previous example, a fundamental interscan time <1.5 ms will be required to characterize the SCP + ICP.

A key advantage of VISTA protocol is that it also generates standard OCTA images, which have been extensively utilized to study retinal diseases. If the maximum interscan time $(N - 1)\Delta t_{fundamental}$ in the OCTA protocol is too short, or α is too small, OCTA will have limited contrast, limiting the VISTA protocol from generating OCTA reliably. The author proposes >50% saturation of OCTA at the longest interscan time, or $\exp[-\alpha(N-1)\Delta t] <0.5$, as a requirement for sufficient OCTA contrast. This yields $\alpha_{min}(N - 1)\Delta t_{fundamental} \approx 0.7$.

Fine sampling density is required in order to resolve capillaries for correct spatial compilation and to achieve a large number of samples. If the A-scan spacing is not fine enough, individual capillaries are less likely to be continuously resolved. With the current SS-OCT system, a ~10 µm or finer A-scan spacing is required to robustly resolve retinal capillaries.

The requirements for the fundamental interscan time and A-scan spacing provide a relationship between the A-scan rate and the maximum FOV for the VISTA protocol. For example, assuming a fundamental interscan time of 1.5 ms, 10 µm A-scan spacing, and 75% scanner duty cycle, a ~530 kHz or higher A-scan rate will be required to achieve 6 mm FOV in the fast scan direction. The A-scan rate requirement can be reduced by sacrificing the fast scan FOV in a linear fashion. Montaging, anisotropic FOVs, using a smaller beam diameter at the pupil to enlarge the beam size at the retina, and improving the scanner duty cycle can also further reduce the A-scan rate requirement. Although a high A-scan rate is required to perform VISTA, smaller FOVs can be assessed using current commercial instruments with 100 to 200 kHz A-scan rates and FOVs can be increased as faster A-scan rates become available.

The framework presented in the second-generation VISTA algorithm can be applied to the general vasculature. Figure 7.1 presents the general summary of VISTA pipeline. Note that spatial compilation approaches other than the vessel segment or cuboid are also possible. For instance, the radial peripapillary capillaries around the optic nerve head (ONH) features a radial orientation, with the ONH at the center. Therefore, disc sectors defined by the angle from the ONH can be adopted as the spatial domain for OCTA compilation. In addition, microaneurysms can be inaccurately segmented if the target radius of OOF is smaller than the size of microaneurysms or the 2D vesselness filter does not have high sensitivity to blob-like structures. In these cases, different segmentation methods, such as deep-learning or manual tracing, can be used to detect microvascular lesions and determine the appropriate spatial domain for OCTA compilation. Still, a chosen spatial domain needs to support the sufficiently large numbers of samples. If the domain does not have enough number of voxels, the saturation characteristic of the domain may be dominated by noise.

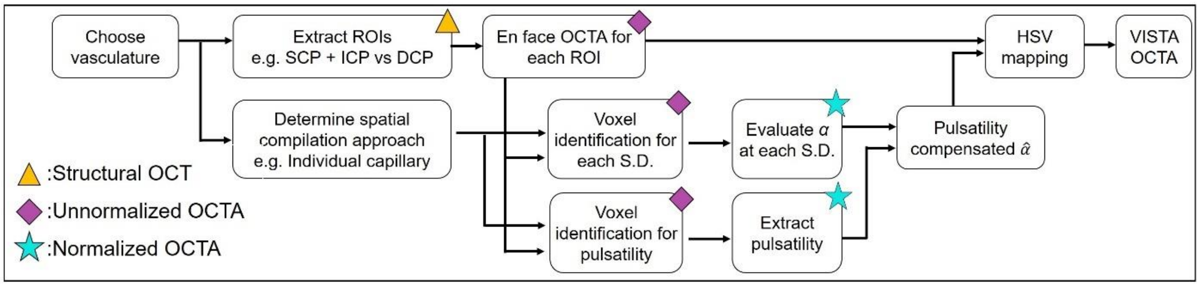

Figure 7.1. VISTA pipeline. S.D.: Spatial domain.

These advances promise to enable clinical studies of blood flow speed alterations in diseases such as diabetic retinopathy and age-related macular degeneration, providing earlier markers of disease, progression and response to therapy.

7.2 Future works

7.2.1 Normal retinal vasculature

The macula has three to four capillary plexuses that are located at different depths, and at least two plexuses at different depths are reported in the posterior pole. Although OCTA can visualize these vasculatures at a capillary level in a depth-resolved manner, the current application of OCTA is mainly in the form of en face 2D images. While this provides an intuitive snapshot of the perfusion status of the vasculature, it does not preserve the information about how the vessel segments are connected to function as a vasculature network. Understanding how the vasculature network supports the retina will require an accurate representation of vasculature as the first step. Optimally oriented flux (OOF) applied on unnormalized OCTA shows that by leveraging the planar shape of projection artifacts, an accurate 3D representation of the vasculature can be reconstructed. This may enable acquiring a 3D graph representation of the vasculature [76].

Since the 3D graph will provide a platform to identify voxels comprising each vessel segment as the 2D graph does, the second-generation VISTA pipeline to evaluate the blood flow speed at capillaries can be applied on the 3D retinal vasculature. This indicates a possibility that i) a complete 3D structural representation of the vasculature and ii) evaluation of the hemodynamics surrogate markers could be achieved from a single OCTA image acquisition. In the adopted OCTA saturation model, $\mathrm{OCTA}(\tau) = \beta\,(1 - \exp(-\alpha\tau))$, β quantifies the ratio of moving red blood cells from the OCT signal. Therefore, β may serve as a surrogate marker for the hematocrit at individual capillaries. Using both β and α, not only the blood flow speed but also blood flow volume rate could be approximated. The intact structural representation of inter-plexus connections enabled by OOF and the blood flow surrogate markers acquired from the 2nd gen VISTA present the opportunity of the first graph representation of the retinal vasculature with hemodynamic information using OCTA.

7.2.2 Normal choroidal vasculature

OCTA on choroidal vasculature poses many challenges (Chapter 6): highly scattering outer retina, the lack of higher reflectivity of the vasculature compared to the surrounding tissue, and the need for accurate segmentation. Here, these challenges are mitigated using a longer 1050 nm wavelength and the robust RPE segmentation enabled by the 3D volume acquisition using inter B-scan registration. Figure 5.3 shows that within a single acquisition, a 600 kHz A-scan rate and 2nd gen VISTA can visualize both the structure and hemodynamics of choriocapillaris using the unnormalized OCTA and the temporal autocorrelation decay constant from normalized OCTA, respectively. While the perfusion of choriocapillaris has been extensively studied with choriocapillaris flow deficit in retinal diseases, how the blood flow speeds of choriocapillaris are different at a various eccentricity have not been characterized in vivo humans. Since the depth resolution of OCTA enables investigation of different layers of choroidal vasculature, the distribution of functional units could be characterized in choriocapillaris and Sattler's layer, respectively.

7.2.3 Diabetic retinopathy

Future studies will include investigating whether $\alpha^{SCP+ICP}$ and α^{DCP} can serve as a reversible biomarker to characterize treatment responses. Currently, anti-VEGF injections are the predominant treatment option for neovascularization in proliferative diabetic retinopathy and diabetic macular edema (DME). However, approximately 40% of eyes with DME show suboptimal responses to this treatment. A biomarker surrogate for the retinal vasculature integrity may offer insights about the edema and its response to anti-VEGF treatment, complementing retinal thickness measurements. This could facilitate risk stratification and expedite alternative treatments for DME.

While the structural imaging of the vasculature from OCTA offers diverse information, it may not be sufficient to characterize anti-VEGF treatment responses. This is underscored by Sorour et al., which showed macula OCTA vessel density did not change post anti-VEGF treatment even when edema showed resolution, and multiple reports indicating reperfusion is unlikely [67, 77].

A compromise of the inner blood retinal barrier is a recognized process behind macular edema. These disruptions could also entail changes in fluid resistance of the vasculature. It is possible that this altered fluid resistance may result in blood flow speed changes, even if the vasculature remains perfused. The VISTA algorithm may be able to provide information about the integrity of inner blood retinal barrier, through blood flow speed changes in the capillary plexuses. If a treatment successfully restores the vascular integrity and subsequently normalizes blood flow speeds in capillaries, then the 2nd gen VISTA might detect these changes, even when non-perfusion areas remain unchanged.

7.2.4 Age-related macular degeneration

Another future study will focus on the development of drusen in age-related macular degeneration (AMD). Drusen, extracellular deposits located between the retinal pigment epithelium (RPE) and Bruch’s membrane, are a clinical hallmark of AMD. OCT structural imaging facilitates the measurement of drusen’s height and volume, providing valuable insights into their progression. Drusen are associated with the advancement to more severe stages of AMD and exhibit various dynamics; they have been reported to collapse spontaneously, expand, newly form, merge with other drusen, change in OCT reflectivity, or remain unchanged. The choriocapillaris, situated beneath the Bruch’s membrane, serves as the interface between the outer retina and the vasculature. Given the nature of drusen as deposits, the choriocapillaris is suspected to play a crucial role in their development. Histological studies have reported a spatial correspondence between drusen formation and choriocapillaris dropout [3].

The second-generation VISTA may enhance our understanding of the relationship between choriocapillaris hemodynamics and drusen development in AMD. Figure 6.3 suggests that blood flow speeds in the choriocapillaris layer are reduced near drusen. Longitudinal imaging studies could investigate the association between the choriocapillaris VISTA blood flow speeds during the initial visit and subsequent drusen growth. A key focus will be comparing blood flow speeds in choriocapillaris in the first visit near the drusen that expanded during the follow-up with those near the drusen that remain unchanged. Additionally, these studies will explore whether choriocapillaris blood flow speed data from the initial visit can predict the formation of new drusen in subsequent follow-up visits.

References

1. I. Bhutto, and G. Lutty, "Understanding age-related macular degeneration (AMD): relationships between the photoreceptor/retinal pigment epithelium/Bruch's membrane/choriocapillaris complex," Molecular Aspects of Medicine **33**, 295-317 (2012).
2. C. Balaratnasingam, D. An, M. Hein, P. Yu, and D.-Y. Yu, "Studies of the retinal microcirculation using human donor eyes and high-resolution clinical imaging: Insights gained to guide future research in diabetic retinopathy," Progress in Retinal and Eye Research **94**, 101134 (2023).
3. R. Lejoyeux, J. Benillouche, J. Ong, M.-H. Errera, E. A. Rossi, S. R. Singh, K. K. Dansingani, S. da Silva, D. Sinha, and J.-A. Sahel, "Choriocapillaris: fundamentals and advancements," Progress in Retinal and Eye Research **87**, 100997 (2022).
4. R. Agrawal, J. Ding, P. Sen, A. Rousselot, A. Chan, L. Nivison-Smith, X. Wei, S. Mahajan, R. Kim, and C. Mishra, "Exploring choroidal angioarchitecture in health and disease using choroidal vascularity index," Progress in Retinal and Eye Research **77**, 100829 (2020).
5. P. A. Campochiaro, "Retinal and choroidal neovascularization," Journal of Cellular Physiology **184**, 301-310 (2000).
6. K. Spilsbury, K. L. Garrett, W.-Y. Shen, I. J. Constable, and P. E. Rakoczy, "Overexpression of vascular endothelial growth factor (VEGF) in the retinal pigment epithelium leads to the development of choroidal neovascularization," The American Journal of Pathology **157**, 135-144 (2000).
7. A. Daruich, A. Matet, A. Moulin, L. Kowalczuk, M. Nicolas, A. Sellam, P.-R. Rothschild, S. Omri, E. Gélizé, L. Jonet, K. Delaunay, Y. D. Kozka, M. Berdugo, M. Zhao, P. Crisanti, and F. Behar-Cohen, "Mechanisms of macular edema: beyond the surface," Progress in Retinal and Eye Research **63**, 20-68 (2018).
8. D. S. McLeod, R. Grebe, I. Bhutto, C. Merges, T. Baba, and G. A. Lutty, "Relationship between RPE and choriocapillaris in age-related macular degeneration," Investigative Ophthalmology & Visual Science **50**, 4982-4991 (2009).
9. A. Biesemeier, T. Taubitz, S. Julien, E. Yoeruek, and U. Schraermeyer, "Choriocapillaris breakdown precedes retinal degeneration in age-related macular degeneration," Neurobiology of Aging **35**, 2562-2573 (2014).
10. J. G. Fujimoto, and D. Huang, "Foreword: 25 years of optical coherence tomography," Investigative Ophthalmology & Visual Science **57**, OCTi-OCTii (2016).
11. D. Huang, E. A. Swanson, C. P. Lin, J. S. Schuman, W. G. Stinson, W. Chang, M. R. Hee, T. Flotte, K. Gregory, and C. A. F. Puliafito, James G, "Optical coherence tomography," Science **254**, 1178-1181 (1991).
12. L. An, and R. K. Wang, "In vivo volumetric imaging of vascular perfusion within human retina and choroids with optical micro-angiography," Optics Express **16**, 11438-11452 (2008).
13. Y. Jia, O. Tan, J. Tokayer, B. Potsaid, Y. Wang, J. J. Liu, M. F. Kraus, H. Subhash, J. G. Fujimoto, J. Hornegger, and D. Huang, "Split-spectrum amplitude-decorrelation angiography with optical coherence tomography," Optics Express **20**, 4710-4725 (2012).
14. R. F. Spaide, J. G. Fujimoto, N. K. Waheed, S. R. Sadda, and G. Staurenghi, "Optical coherence tomography angiography," Progress in Retinal and Eye Research **64**, 1-55 (2018).
15. R. F. Spaide, J. G. Fujimoto, and N. K. Waheed, "Image artifacts in optical coherence angiography," Retina **35**, 2163 (2015).

16. M. Zhang, T. S. Hwang, J. P. Campbell, S. T. Bailey, D. J. Wilson, D. Huang, and Y. Jia, "Projection-resolved optical coherence tomographic angiography," Biomedical Optics Express **7**, 816-828 (2016).
17. S. Yazdanfar, A. M. Rollins, and J. A. Izatt, "Imaging and velocimetry of the human retinal circulation with color Doppler optical coherence tomography," Optics Letters **25**, 1448-1450 (2000).
18. B. Lee, E. A. Novais, N. K. Waheed, M. Adhi, E. Talisa, E. D. Cole, E. M. Moult, W. Choi, M. Lane, and C. R. Baumal, "En face Doppler optical coherence tomography measurement of total retinal blood flow in diabetic retinopathy and diabetic macular edema," JAMA Ophthalmology **135**, 244-251 (2017).
19. I. Laíns, J. C. Wang, Y. Cui, R. Katz, F. Vingopoulos, G. Staurenghi, D. G. Vavvas, J. W. Miller, and J. B. Miller, "Retinal applications of swept source optical coherence tomography (OCT) and optical coherence tomography angiography (OCTA)," Progress in Retinal and Eye Research **84**, 100951 (2021).
20. T. S. Hwang, S. S. Gao, L. Liu, A. K. Lauer, S. T. Bailey, C. J. Flaxel, D. J. Wilson, D. Huang, and Y. Jia, "Automated quantification of capillary nonperfusion using optical coherence tomography angiography in diabetic retinopathy," JAMA Ophthalmology **134**, 367-373 (2016).
21. Y. Jia, S. T. Bailey, D. J. Wilson, O. Tan, M. L. Klein, C. J. Flaxel, B. Potsaid, J. J. Liu, C. D. Lu, M. F. Kraus, J. G. Fujimoto, and D. Huang, "Quantitative optical coherence tomography angiography of choroidal neovascularization in age-related macular degeneration," Ophthalmology **121**, 1435-1444 (2014).
22. N. Hasegawa, M. Nozaki, N. Takase, M. Yoshida, and Y. Ogura, "New insights into microaneurysms in the deep capillary plexus detected by optical coherence tomography angiography in diabetic macular edema," Investigative Ophthalmology & Visual Science **57**, OCT348-OCT355 (2016).
23. P. L. Nesper, P. K. Roberts, A. C. Onishi, H. Chai, L. Liu, L. M. Jampol, and A. A. Fawzi, "Quantifying microvascular abnormalities with increasing severity of diabetic retinopathy using optical coherence tomography angiography," Investigative Ophthalmology & Visual Science **58**, BIO307-BIO315 (2017).
24. M. Ashraf, K. Sampani, A. Clermont, O. Abu-Qamar, J. Rhee, P. S. Silva, L. P. Aiello, and J. K. Sun, "Vascular density of deep, intermediate and superficial vascular plexuses are differentially affected by diabetic retinopathy severity," Investigative Ophthalmology & Visual Science **61**, 53-53 (2020).
25. A. Couturier, P.-A. Rey, A. Erginay, C. Lavia, S. Bonnin, B. Dupas, A. Gaudric, and R. Tadayoni, "Widefield OCT-angiography and fluorescein angiography assessments of nonperfusion in diabetic retinopathy and edema treated with anti–vascular endothelial growth factor," Ophthalmology **126**, 1685-1694 (2019).
26. V. Schreur, A. Domanian, B. Liefers, F. G. Venhuizen, B. J. Klevering, C. B. Hoyng, E. K. de Jong, and T. Theelen, "Morphological and topographical appearance of microaneurysms on optical coherence tomography angiography," British Journal of Ophthalmology **103**, 630-635 (2019).
27. S. Parrulli, F. Corvi, M. Cozzi, D. Monteduro, F. Zicarelli, and G. Staurenghi, "Microaneurysms visualisation using five different optical coherence tomography angiography devices compared to fluorescein angiography," British Journal of Ophthalmology **105**, 526-530 (2021).

28. M. Arya, O. Sorour, J. Chaudhri, Y. Alibhai, N. K. Waheed, J. S. Duker, and C. R. Baumal, "Distinguishing intraretinal microvascular abnormalities from retinal neovascularization using optical coherence tomography angiography," Retina **40**, 1686-1695 (2020).
29. D. WuDunn, H. L. Takusagawa, A. J. Sit, J. A. Rosdahl, S. Radhakrishnan, A. Hoguet, Y. Han, and T. C. Chen, "OCT angiography for the diagnosis of glaucoma: A report by the American Academy of Ophthalmology," Ophthalmology **128**, 1222-1235 (2021).
30. J. R. de Oliveira Dias, Q. Zhang, J. M. Garcia, F. Zheng, E. H. Motulsky, L. Roisman, A. Miller, C.-L. Chen, S. Kubach, and L. de Sisternes, "Natural history of subclinical neovascularization in nonexudative age-related macular degeneration using swept-source OCT angiography," Ophthalmology **125**, 255-266 (2018).
31. M. Thulliez, Q. Zhang, Y. Shi, H. Zhou, Z. Chu, L. de Sisternes, M. K. Durbin, W. Feuer, G. Gregori, and R. K. Wang, "Correlations between choriocapillaris flow deficits around geographic atrophy and enlargement rates based on swept-source OCT imaging," Ophthalmology Retina **3**, 478-488 (2019).
32. J. Lee, W. Wu, J. Y. Jiang, B. Zhu, and D. A. Boas, "Dynamic light scattering optical coherence tomography," Optics Express **20**, 22262-22277 (2012).
33. Y. Wang, and R. Wang, "Autocorrelation optical coherence tomography for mapping transverse particle-flow velocity," Optics Letters **35**, 3538-3540 (2010).
34. A. S. Nam, B. Braaf, and B. J. Vakoc, "Using the dynamic forward scattering signal for optical coherence tomography based blood flow quantification," Optics Letters **47**, 3083-3086 (2022).
35. J. Tokayer, Y. Jia, A.-H. Dhalla, and D. Huang, "Blood flow velocity quantification using split-spectrum amplitude-decorrelation angiography with optical coherence tomography," Biomedical Optics Express **4**, 1909-1924 (2013).
36. W. Choi, E. M. Moult, N. K. Waheed, M. Adhi, B. Lee, C. D. Lu, E. Talisa, V. Jayaraman, P. J. Rosenfeld, J. S. Duker, and J. G. Fujimoto, "Ultrahigh-speed, swept-source optical coherence tomography angiography in nonexudative age-related macular degeneration with geographic atrophy," Ophthalmology **122**, 2532-2544 (2015).
37. S. B. Ploner, E. M. Moult, W. Choi, N. K. Waheed, B. Lee, E. A. Novais, E. D. Cole, B. Potsaid, L. Husvogt, J. Schottenhamml, A. Maier, P. J. Rosenfeld, J. S. Duker, J. Hornegger, and J. G. Fujimoto, "Toward quantitative optical coherence tomography angiography: visualizing blood flow speeds in ocular pathology using variable interscan time analysis," Retina **36**, S118-S126 (2016).
38. C. B. Rebhun, E. M. Moult, E. A. Novais, C. Moreira-Neto, S. B. Ploner, R. N. Louzada, B. Lee, C. R. Baumal, J. G. Fujimoto, J. S. Duker, N. K. Waheed, and D. Ferrara, "Polypoidal choroidal vasculopathy on swept-source optical coherence tomography angiography with variable interscan time analysis," Translational Vision Science & Technology **6**, 4-4 (2017).
39. M. Arya, M. Bonini Filho, C. B. Rebhun, E. M. Moult, B. Lee, Y. Alibhai, A. J. Witkin, C. R. Baumal, J. S. Duker, J. G. Fujimoto, and N. K. Waheed, "Analyzing Relative Flow Speeds in Diabetic Retinopathy Using Variable Interscan Time Analysis OCT Angiography," Ophthalmology Retina **5**, 49-59 (2021).
40. C. B. Rebhun, E. M. Moult, S. B. Ploner, C. M. Neto, A. Y. Alibhai, J. Schottenhamml, B. Lee, W. Choi, F. A. Rifai, M. W. Tam, L. Husvogt, C. R. Baumal, A. J. Witkin, A. Maier, P. J. Rosenfeld, J. S. Duker, J. G. Fujimoto, and N. K. Waheed, "Analyzing relative blood

flow speeds in choroidal neovascularization using variable interscan time analysis OCT angiography," Ophthalmology Retina **2**, 306-319 (2018).

41. S. A. Burns, A. E. Elsner, K. A. Sapoznik, R. L. Warner, and T. J. Gast, "Adaptive optics imaging of the human retina," Progress in Retinal and Eye Research **68**, 1-30 (2019).
42. S. A. Burns, A. E. Elsner, and T. J. Gast, "Imaging the retinal vasculature," Annual Review of Vision Science **7**, 129 (2021).
43. R. L. Warner, A. de Castro, L. Sawides, T. Gast, K. Sapoznik, T. Luo, and S. A. Burns, "Full-field flicker evoked changes in parafoveal retinal blood flow," Scientific Reports **10**, 1-10 (2020).
44. A. de Castro, G. Huang, L. Sawides, T. Luo, and S. A. Burns, "Rapid high resolution imaging with a dual-channel scanning technique," Optics Letters **41**, 1881-1884 (2016).
45. B. Gu, X. Wang, M. D. Twa, J. Tam, C. A. Girkin, and Y. Zhang, "Noninvasive in vivo characterization of erythrocyte motion in human retinal capillaries using high-speed adaptive optics near-confocal imaging," Biomedical Optics Express **9**, 3653-3677 (2018).
46. P. Bedggood, and A. Metha, "Mapping flow velocity in the human retinal capillary network with pixel intensity cross correlation," PLOS One **14**, e0218918 (2019).
47. P. Bedggood, and A. Metha, "Direct measurement of pulse wave propagation in capillaries of the human retina," Optics Letters **46**, 4450-4453 (2021).
48. W. Choi, B. Potsaid, V. Jayaraman, B. Baumann, I. Grulkowski, J. J. Liu, C. D. Lu, A. E. Cable, D. Huang, and J. S. Duker, "Phase-sensitive swept-source optical coherence tomography imaging of the human retina with a vertical cavity surface-emitting laser light source," Optics Letters **38**, 338-340 (2013).
49. J. Zhang, T. Nguyen, B. Potsaid, V. Jayaraman, C. Burgner, S. Chen, J. Li, K. Liang, A. Cable, and G. Traverso, "Multi-MHz MEMS-VCSEL swept-source optical coherence tomography for endoscopic structural and angiographic imaging with miniaturized brushless motor probes," Biomedical Optics Express **12**, 2384-2403 (2021).
50. S. Chen, B. Potsaid, Y. Li, J. Lin, Y. Hwang, E. M. Moult, J. Zhang, D. Huang, and J. G. Fujimoto, "High speed, long range, deep penetration swept source OCT for structural and angiographic imaging of the anterior eye," Scientific Reports **12**, 1-14 (2022).
51. M. Guizar-Sicairos, S. T. Thurman, and J. R. Fienup, "Efficient subpixel image registration algorithms," Optics Letters **33**, 156-158 (2008).
52. Y. Jia, J. M. Simonett, J. Wang, X. Hua, L. Liu, T. S. Hwang, and D. Huang, "Wide-field OCT angiography investigation of the relationship between radial peripapillary capillary plexus density and nerve fiber layer thickness," Investigative Ophthalmology & Visual Science **58**, 5188-5194 (2017).
53. J. Lee, J. Y. Jiang, W. Wu, F. Lesage, and D. A. Boas, "Statistical intensity variation analysis for rapid volumetric imaging of capillary network flux," Biomedical Optics Express **5**, 1160-1172 (2014).
54. M. W. Law, and A. C. Chung, "Three dimensional curvilinear structure detection using optimally oriented flux," in *Computer Vision–ECCV 2008: 10th European Conference on Computer Vision, Marseille, France, October 12-18, 2008, Proceedings, Part IV 10*(Springer2008), pp. 368-382.
55. T. Jerman, F. Pernuš, B. Likar, and Ž. Špiclin, "Enhancement of vascular structures in 3D and 2D angiographic images," IEEE Transactions on Medical Imaging **35**, 2107-2118 (2016).

56. P. Kollmannsberger, M. Kerschnitzki, F. Repp, W. Wagermaier, R. Weinkamer, and P. Fratzl, "The small world of osteocytes: connectomics of the lacuno-canalicular network in bone," New Journal of Physics **19**, 073019 (2017).
57. A. Avanaki, K. Espig, T. Kimpe, A. Xthona, C. Marchessoux, J. Rostang, and B. Piepers, "Perceptual uniformity of commonly used color spaces," in *Medical Imaging 2014: Digital Pathology*(SPIE2014), pp. 198-203.
58. G. Paschos, "Perceptually uniform color spaces for color texture analysis: an empirical evaluation," IEEE Transactions on Image Processing **10**, 932-937 (2001).
59. D. Borland, and R. M. T. Ii, "Rainbow color map (still) considered harmful," IEEE Computer Graphics and Applications **27**, 14-17 (2007).
60. R. L. Warner, T. J. Gast, K. A. Sapoznik, A. Carmichael-Martins, and S. A. Burns, "Measuring Temporal and Spatial Variability of Red Blood Cell Velocity in Human Retinal Vessels," Investigative Ophthalmology & Visual Science **62**, 29-29 (2021).
61. R. Lee, T. Y. Wong, and C. Sabanayagam, "Epidemiology of diabetic retinopathy, diabetic macular edema and related vision loss," Eye and Vision **2**, 1-25 (2015).
62. D. A. Antonetti, R. Klein, and T. W. Gardner, "Diabetic Retinopathy," New England Journal of Medicine **366**, 1227-1239 (2012).
63. Q. Zhang, C. S. Lee, J. Chao, C.-L. Chen, T. Zhang, U. Sharma, A. Zhang, J. Liu, K. Rezaei, and K. L. Pepple, "Wide-field optical coherence tomography based microangiography for retinal imaging," Scientific Reports **6**, 22017 (2016).
64. K. B. Schaal, M. R. Munk, I. Wyssmueller, L. E. Berger, M. S. Zinkernagel, and S. Wolf, "Vascular abnormalities in diabetic retinopathy assessed with swept-source optical coherence tomography angiography widefield imaging," Retina **39**, 79-87 (2019).
65. J. F. Russell, and I. C. Han, "Toward a new staging system for diabetic retinopathy using wide field swept-source optical coherence tomography angiography," Current Diabetes Reports **21**, 1-11 (2021).
66. B. Tombolini, E. Borrelli, R. Sacconi, F. Bandello, and G. Querques, "Diabetic macular ischemia," Acta Diabetologica **59**, 751-759 (2022).
67. C. C. Wykoff, H. J. Yu, R. L. Avery, J. P. Ehlers, R. Tadayoni, and S. R. Sadda, "Retinal non-perfusion in diabetic retinopathy," Eye **36**, 249-256 (2022).
68. M. Fleckenstein, T. D. Keenan, R. H. Guymer, U. Chakravarthy, S. Schmitz-Valckenberg, C. C. Klaver, W. T. Wong, and E. Y. Chew, "Age-related macular degeneration," Nature Reviews Disease Primers **7**, 31 (2021).
69. K. N. Khan, O. A. Mahroo, R. S. Khan, M. D. Mohamed, M. McKibbin, A. Bird, M. Michaelides, A. Tufail, and A. T. Moore, "Differentiating drusen: Drusen and drusen-like appearances associated with ageing, age-related macular degeneration, inherited eye disease and other pathological processes," Progress in retinal and eye research **53**, 70-106 (2016).
70. F. G. Holz, T. J. Wolfensberger, B. Piguet, M. Gross-Jendroska, J. A. Wells, D. C. Minassian, I. H. Chisholm, and A. C. Bird, "Bilateral macular drusen in age-related macular degeneration: prognosis and risk factors," Ophthalmology **101**, 1522-1528 (1994).
71. M. Veerappan, A.-K. M. El-Hage-Sleiman, V. Tai, S. J. Chiu, K. P. Winter, S. S. Stinnett, T. S. Hwang, G. B. Hubbard III, M. Michelson, and R. Gunther, "Optical coherence tomography reflective drusen substructures predict progression to geographic atrophy in age-related macular degeneration," Ophthalmology **123**, 2554-2570 (2016).

72. Z. Chu, Q. Zhang, G. Gregori, P. J. Rosenfeld, and R. K. Wang, "Guidelines for imaging the choriocapillaris using OCT angiography," American Journal of Ophthalmology **222**, 92-101 (2021).
73. R. F. Spaide, "Choriocapillaris flow features follow a power law distribution: implications for characterization and mechanisms of disease progression," American Journal of Ophthalmology **170**, 58-67 (2016).
74. M. Nassisi, E. Baghdasaryan, T. Tepelus, S. Asanad, E. Borrelli, and S. R. Sadda, "Topographic distribution of choriocapillaris flow deficits in healthy eyes," PloS One **13**, e0207638 (2018).
75. Y. Hwang, J. Won, A. Yaghy, H. Takahashi, J. M. Girgis, K. Lam, S. Chen, E. M. Moult, S. B. Ploner, and A. Maier, "Retinal blood flow speed quantification at the capillary level using temporal autocorrelation fitting OCTA," Biomedical Optics Express **14**, 2658-2677 (2023).
76. K. W. Walek, S. Stefan, J.-H. Lee, P. Puttigampala, A. H. Kim, S. W. Park, P. J. Marchand, F. Lesage, T. Liu, and Y.-W. A. Huang, "Near-lifespan longitudinal tracking of brain microvascular morphology, topology, and flow in male mice," Nature Communications **14**, 2982 (2023).
77. O. A. Sorour, A. S. Sabrosa, A. Yasin Alibhai, M. Arya, A. Ishibazawa, A. J. Witkin, C. R. Baumal, J. S. Duker, and N. K. Waheed, "Optical coherence tomography angiography analysis of macular vessel density before and after anti-VEGF therapy in eyes with diabetic retinopathy," International Ophthalmology **39**, 2361-2371 (2019).